A three dimensional automated testing platform for 3D magnetic sensors

BSc Thesis

EE3L11 Bachelor Graduation Project Electrical Engineering

Toby van Hooff & Angelie Repriels

Delft University of Technology

TU Delft

A three dimensional automated testing platform for 3D magnetic sensors

BSc Thesis

by

Toby van Hooff & Angelie Repriels

Supervisor: Dr. Karen Dowling
Project Duration: April, 2025 - June, 2025
Faculty: Faculty of Electrical Engineering, Mathematics & Computer Science, Delft

TU Delft

Abstract

Currently, the testing procedure for 3D Hall sensors at the MUSIC lab is time-consuming, labour-intensive, and is susceptible to systematic errors. There is a need for an automated, accurate, and repeatable test setup for 3D magnetic sensor characterisation. That is why the objective of this thesis is to develop a control interface that allows users to define arbitrary magnetic field vectors and perform 3D magnetic field sweeps on a Hall sensor placed in a 3D Helmholtz coil. The development was performed in three stages: calibration of a 3D Helmholtz coil, development of a 3D magnetic field sweeping script, and validation of the system by benchmarking measurements from two commercially available 3D Hall sensors against known magnetic fields. The 3D Helmholtz coil was successfully calibrated, finding that the generated magnetic field strength of 2.87mT corresponds to the maximum relative uncertainty of 2%. A LabVIEW script was developed, enabling users to generate 3D static magnetic field vectors and 3D magnetic field sweeps with definable orientation, resolution and strength. Lastly, the system was validated using two commercial Hall sensors, confirming its stability and accuracy for testing other Hall sensors. This system can be used for repeatable magnetic sensor evaluation in research, with a versatility that can benefit various sensor configurations.

Preface

This project is the final step of our Bachelors degree and has been a valuable learning experience. It has taught us a lot, not only technical skills regarding magnetic sensor testing, LabVIEW, and hardware control, but also troubleshooting and patience.

We would like to thank our supervisor, Dr. Karen Dowling, for her guidance during the project. She provided timely support while also allowing us the independence to shape the project in our own way. We would also like to thank Jacopo Ruggeri and Lex Pardon for their help during the a challenging part of the project, when we encountered issues with power supply communication via LabVIEW. Lastly, we would like to thank Francis Voordenhout and Tycho Brouwer for developing the magnetic sensor readout interface and 3D printing a range of sensor supports for us. Thank you to everyone who contributed to making this project a meaningful part of our studies.

Toby van Hooff & Angelie Repriels
Delft, June 2025

Contents

1 Introduction

1.1. Problem definition

3D Magnetic sensing is incredibly useful for navigation, power electronic current monitoring, and position sensing in controller joysticks, wheels, and robotics. 3D magnetic sensing with Hall sensors can be obtained by integrating three one-dimensional (1D) Hall sensors on the same platform [1]. Such a device suffers from crosstalk (unwanted interaction between elements) between the dimensions, causing a lower signal to noise ratio than achieved in 1D sensors. Furthermore, they must be calibrated such that their sensitivities are equal, having an isometric response. If there are angular errors in the placement of the individual sensors, this also strongly contributes to the cross-sensitivity in the device.

TU Delft is home to a novel 3D magnetic sensor based on a pyramid structure, with a micro-machined surface. This sensor demonstrates high isotropy and sensitivity competitive with state of the art Hall effect 3D sensors. Currently, this sensor is being tested utilising a constant one-dimensional magnetic field and requires the sensor to be physically rotated to complete the full calibration process across all directions. However, this testing process is extremely time-consuming and labour-intensive. Moreover, it suffers from systematic errors due to angular misalignment, which stem from imperfect mechanical rotation and possible misalignment between the rotation axis and the intended measurement axis. The experimental characterization conducted by Ruggeri et al. reported an angular rotation error of approximately 3° [2].

There is a need for an automated, accurate, and repeatable test setup for 3D magnetic sensor characterisation. This thesis aims to develop a system that replaces mechanical rotation of sensors with automated magnetic field generation using a 3D Helmholtz coil. The 3D Hall sensor can be placed in the centre of the 3D Helmholtz coil, which generates specific magnetic field strengths by precisely controlling the coil currents. This method doesn't involve mechanical movement of the sensor, which reduces geometric and alignment errors and can lead to higher accuracy.

The main objective of this thesis is to develop and validate a control interface that allows users to define arbitrary magnetic field vectors and perform 3D magnetic field sweeps. Before the 3D magnetic test setup can be used for sensor characterisation, the 3D Helmholtz coil system must be calibrated. This results in a relationship between the input coil currents and the resulting magnetic field strength at the centre of the coils. Accurate calibration is essential to ensure the generated fields match the desired field strength with high accuracy. Then, the system should be able to perform automated 3D magnetic field sweeps. The number of steps to take, sweeping plane, vector orientation, and magnetic field strength can be defined by the user, making the setup versatile for characterizing a wide range of sensor behaviours.

To validate the accuracy of the system, measurements of two commercial 3D Hall sensors will be benchmarked against known magnetic fields. If the sensor measurements yield consistent and expected results, the test setup can be verified. Project success is evaluated according to the requirements defined in the Program of Requirements (chapter 2). The sensitivity of the sensors are evaluated, compared

to each other, and validated according to their specifications provided by their data sheets.

1.2. Thesis outline

This thesis is structured as follows. Section 1.3 is a state-of-the art analysis, outlining the background necessary to understand the context of this work. Chapter 2 covers the Programme of Requirements, presenting the functional and system requirements of this work. Chapter 3 discusses the calibration of the 3D Helmholtz coil system. Chapter 4 covers the functionality, development, structure, and validation of the LabVIEW script for 3D magnetic field sweeping. Chapter 5 discusses the sensor characterisation measurements and validates the script. Chapter 6 discusses the results and their implications. Finally, chapter 7 draws conclusions and offers recommendations for future work.

1.3. State-of-the-art analysis

This state-of-the-art analysis is divided in two parts. First, subsection 1.3.1 discusses working principles of Hall-effect sensors. It then reviews the most commonly used types, namely the 3D magnetic sensor utilising Planar and Vertical Hall Devices. Finally, it briefly introduces the pyramid 3-axis silicon Hall-effect magnetic sensor developed by the MUSIC lab. Next, subsection 1.3.2 discusses the testing protocols for 3D magnetic sensors. First focussing on the ways that a magnetic field can be generated, highlighting the advantages of using a Helmholtz coil. Then, it discusses how sensors are characterised using the magnetic field produced by a 3D Helmholtz coil setup.

1.3.1. 3D Hall-effect magnetic sensors

Working principle hall-effect sensors

A Hall-effect sensor is a type of magnetic sensor that produces an output voltage in response to an incident magnetic field, a phenomenon known as the Hall effect. This magnetic field should be out of plane with the device, ideally orthogonal to it. Hall effect sensors are typically made of semiconductor material, where n-type material is favoured. Figure 1.1 (left) shows a sideview of the way a Hall device can be constructed using semiconductor material. The n-well is surrounded by a p-type substrate, and the contacts are made of n-type as well, only higher doped than the well. In general, a relatively low doped material is used, as the sensitivity of the device drops as the doping concentration increases.

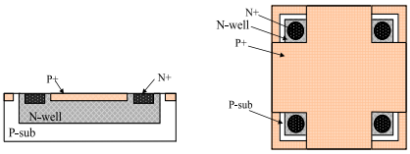

Figure 1.1: 1D Hall device [3]

A 1D Hall sensor commonly has 4 contacts, as shown in Figure 1.1 (right). 2 contacts on one of the diagonals are used for the electrical energy supply, and the other 2 are used to measure the Hall voltage. Current flows from one contact diagonally over the plate to another contact. A magnetic field B exerts a Lorentz force on a moving charge q. The Lorentz force causes the current to deflect to one side of the conductor, creating a Hall voltage V_H, which is perpendicular to both the current and the magnetic field, and can be measured using the other two contacts. The Hall voltage is proportional to the magnetic field strength, as shown in Equation 1.1, where *I* is the current, *B* the magnetic field strength, n the carrier concentration, q the moving electric charge, and d the thickness of the conductor [4].

$$V_H = \frac{IB}{nqd} \tag{1.1}$$

To characterise a Hall device, a metric used to quantify the response of the Hall voltage to the magnetic field is the absolute sensitivity S_A in V/T[4]. There are numerous benefits to using Hall effect sensors for magnetic sensing [4], [5]. Firstly, the architecture of the device is simple and robust, allowing easy manufacturing and ensuring low costs. The construction is also easily repeatable, and it is highly similar to microelectronics fabrication, so integration with CMOS circuits is possible. Lastly, the device

produces a linear response, which makes it straightforward to work with. However, the device also has some shortcomings. The output signal can be weak when compared to other types of magnetic sensors. The device is also sensitive to temperature. Moreover, at zero applied magnetic field, there is be a quasi-static offset voltage V_{off} present at the output terminal, that varies with temperature and time [4].

3D Hall-effect magnetic sensors

Whereas a 1D Hall sensor can only sense the field strength in one direction, many applications require the field to be known in two or three dimensions. This requires a sensor that can reconstruct the entire magnetic field vector, which is more complex. As mentioned before, a 3D sensor can be composed of three 1D sensors, at the cost of lower signal to noise ratio due to crosstalk between the 3 elements. If there are angular errors in the placement of the individual sensors, this strongly contributes to the cross-sensitivity in the device. In this section the 3D magnetic sensor utilising Planar and Vertical Hall Devices, and the pyramid 3-axis silicon Hall effect magnetic sensor are presented.

A sensor measuring a 3D field using 3 1D Hall devices consists of one Planar Hall Device (PHD) and two Vertical Hall Devices (VHD). They detect magnetic fields perpendicular and parallel to the device, respectively. Planar Hall Devices work the same as the 1D Hall device described in subsection 1.3.1. Vertical Hall Devices are a bit more complicated, as they have to measure parallel magnetic fields. In the leftmost figure of 1.2, the PHD measures the magnetic field in the z direction, while the VHDs measure the field in the x and y direction.

Both types of devices have a large offset. VHDs have asymmetrical electric properties, which makes offset correction more difficult [6]. When integrating the VHDs and PHD to create a 3D hall sensor, the parameters of all three devices must be optimized such that they have the same performance. Matching the performance of the VHDs to that of the PHD to achieve this is quite challenging. There is a trade-off between sensitivity and offset in 3D hall devices that use VHDs [6].

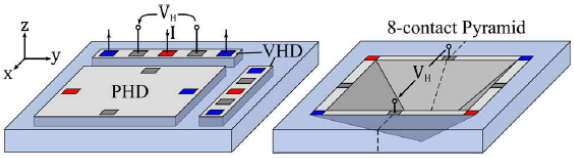

Figure 1.2: Illustration of the physical structure of a 3D pyramid Hall sensor (right) and a typical CMOS integrated 3D Hall sensor (left) [1].

Contrary to these standard 3D Hall devices, the pyramid 3-axis silicon Hall effect magnetic sensor achieves a higher sensitivity [1]. Whereas most CMOS integrated 3D Hall sensors use multiple surfaces to sense in different directions, this configuration uses just one surface to sense in all three directions. The structure of the pyramid sensor compared to a sensor consisting of a planar and vertical hall devices is presented in Figure 1.2.

While this configuration of a 3D Hall sensor provides great sensitivity in integrated CMOS technology, it does have some offset that must be dealt with. This can be done by using the current spinning method for each of the three sensing modes [2].

1.3.2. Testing protocols for 3D magnetic sensors

3D Hall effect sensors are prone to axes misalignment due manufacturing tolerances and installation inaccuracies. This significantly reduces the accuracy of measurement results. Therefore, the sensor must be calibrated before use to ensure that the measurement of the stand-alone sensor corresponds to the actual value of the magnetic field [7]. In other words, the goal of calibration is to establish the Hall effect sensor's voltage-to-magnetic-field characteristic in all three directions (x, y, z), and the sensor's cross-sensitivity.

The calibration of any 3D Hall sensor requires a homogeneous magnetic field that can be varied in strength and direction, and a reference probe [8]. The sensor is placed in a magnetic field and the output

voltage is measured. The magnetic field must be known, controlled, and uniform. There are two widely used methods to generate the magnetic field: permanent magnets or a Helmholtz coil. Each method has its advantages and disadvantages. Beyond these traditional methods, other calibration techniques are possible too. Rotating magnets or coils mounted on a robotic arm can sweep the magnetic field across different magnitudes and directions. Alternatively, magnet arrays can be rotated to produce complex magnetic fields. These alternative methods often involve greater mechanical complexity or require real-time field measurement systems for feedback control, thus are less advantageous.

Appendix A discusses the magnetic field generated by a permanent magnet, and covers the magnetic field generated by a uni-axial Helmholtz coil and a three-axial Helmholtz coil, respectively. It is discussed that a permanent magnet can provide very strong magnetic fields, ranging from $0.1T$ to $1T$, depending material and size. However, the field is highly non-uniform and sensitive to alignment on the central axis. This makes it less ideal for sensor calibration. Additionally, this non-uniformity is particularly problematic if testing is done in three dimensions, which limits its suitability for calibration of 3D Hall sensors. While the magnetic field strength of a Helmholtz coil isn't as big, generally around tens to hundreds of mT depending on coil design and applied current, it is still more suitable for sensor testing as the field is highly uniform and linear in a specified region.
To take full advantage of the controlled, uniform magnetic field, accurate calibration methods are essential. There are two common calibration methods: scalar calibration and vector calibration.

Scalar calibration is the most commonly used method. It utilises a constant, stable magnetic field and requires the sensor to be physically rotated to complete the full calibration process. A one-dimensional Helmholtz coil can be used for this method, as it produces a uniform magnetic field in one direction. This method suffers from systematic errors due to angular misalignment, which stem from imperfect mechanical rotation and possible misalignment between the rotation axis and the intended measurement axis. Furthermore, creating a precise mathematical model is difficult and the setup cannot ignore the fluctuation and inhomogeneity of the magnetic field, making accurate correction of the components difficult to achieve [9].

Contrary to scalar calibration, vector calibration uses a high-precision magnetic field generator to generate controlled magnetic field that can be varied in strength and direction, which is used as a reference for calibrating the sensor [9]. This controlled, three-dimensional magnetic field is created by a 3D Helmholtz coil. The first step of this method involves placing a 3D Hall-effect sensor in the centre of the 3D Helmholtz coil, with the centre of the sensor aligned with the centre of the coil. The three axis of the sensor and the axis of the coil should be arranged in the same direction. Once the experimental platform is set up, a large set of excitation currents of different directions and magnitudes are added to the three axes of the coil by controlling the coil current source, and the corresponding measured values of the sensors are recorded [9]. From this data, the sensitivity and sensor errors can be calculated. Correction of these errors can be achieved through various techniques, including machine learning-based sensor vector correction methods [9].

2

Programme of requirements

The goal of this project is to provide an automated 3D magnetic field test set up. This entails calibrating a 3D Helmholtz coil and developing a LabVIEW script that automates the 3D field sweeping. This setup is then utilised this to benchmark two commercial 3D Hall-effect sensor chips and compare their outputs. This automated test setup will be used by the MUSIC lab to test the inverted pyramid 3-axis silicon Hall effect magnetic sensor, and the benchmarking results will be used to compare the performance of commercially available Hall effect sensors with the TU Delft's pyramid structured 3D Hall effect sensor. The requirements of the system can be divided into several parts. The functional requirements concern the purpose of the product to be developed, and are as follows:

[1.1] The calibration of the 3D Helmholtz coil should result in a relationship between the current applied to the coils and the resulting magnetic field strength.

[1.2] The script must execute a 3D magnetic field sweep over user-defined magnetic field ranges and vector orientation across all octants. It must allow the user to choose the sweep resolution and advance each step via a button press.

[1.3] The script must log the current system state, which includes the voltage, current, and magnetic field strength for each coil, at approximately 10-second intervals. Each log must include a timestamp and be logged in an Excel file.

[1.4] The sensor characterisation must record the output voltages of the sensor for the x, y, and z directions over the magnetic field range of the 3D Helmholtz coil. So, it should display the sensitivities of the sensors in each direction.

[1.5] The sensor characterisation must record the output voltages in x, y, and z direction during an angular sweep of the magnetic field, and should be visualised with error plots.

The ecological embedding in the environment requirements entail environment, safety (in operation), social aspects, esthetics, logistics, etc. These are as follows:

[2.1] The presence of magnetic materials near the Helmholtz coil should be prevented, as they can distort the generated magnetic field.

System requirements concern the main features and functionalities to be implemented, with the pertaining performance indicators. These are as follows:

[3.1] The magnetic field uniformity of the 3D Helmholtz coil in the central 20 mm sphere must be validated to have at most 1% deviation.

[3.2] Since sensor noise, temperature fluctuations, and minor misalignments of the sensor and Gauss probe can lead to deviations, each measurement must be repeated at least 3 times. More measurements must be taken if operational factors have affected the sensor output, or the standard deviation between measurements exceeds 4%.

[3.3] The magnetic field generated by the coils must be stable to ±1 μT for the duration of 30 minutes.

[3.4] The calibration of the coils must result in a current-to-magnetic field relationship with an uncertainty of no more than 2%. This ensures that the magnetic field sweep script operates with a maximum inaccuracy of 2% during sweeps.

[3.5] The 3D field sweeping script must support magnetic field settings from 0 mT to 7 mT on each axis, with a user-defined resolution. It must be sweepable from 0° to 360° in a user-defined defined plane.

[3.6] During the characterisation, distinct magnetic field strengths in each Cartesian direction ranging from -7 mT to 7 mT should be applied to each sensor. The spacing should be chosen such that the field increment is at least more than double the sensor's resolution.

Lastly, the development of manufacturing methodologies requirements cover the dedicated tools, devices, testing facilities, supporting equipment, etc.

[4.1] The calibration of the Helmholtz coil must be done with a standard Gauss meter.

[4.2] The automated 3D field sweeping script must be developed in LabVIEW.

[4.3] The sensor characterisation must be performed with the calibrated Helmholtz coil and developed LabVIEW sweeping script.

3

Calibration of a 3D Helmholtz Coil with a standard Gauss meter

This chapter discusses the calibration of the 3D Helmholtz coil and presents the results. Section 3.1 presents the equipment and measurements instruments that are used. Next, section 3.2 analyses the heating effects in the coils. Then the main part of the calibration is discussed in section 3.3, namely determining the relationship between the applied current and the created magnetic field. Next, section 3.4 validates the uniformity in the centre of the Helmholtz coil. Lastly, section 3.5 presents a conclusion on the accuracy and stability of the magnetic field created in the Helmholtz coil.

3.1. Equipment and measurement instruments

The three-axial Helmholtz coil used in this project is the 3DXHC4-70 model, fabricated by Xiamen Dexing Magnet Tech. Co., Ltd. The z-axis coil pair has an equivalent diameter of 80 mm, the y-axis coil pair has an equivalent diameter of 164 mm, and the x-axis coil pair is the largest with an equivalent diameter of 260 mm, enclosing the other two pairs. The magnetic field produced by each coil pair is in the range 0 to 7 mT. According to the performance test report, the diameter of the uniformity sphere is 20 mm, where the z-component of the magnetic field has a 0.45 % uniformity error, the y-component 0.08%, and the x-component 0.02%. Lastly, due to thermal limits of the coils the maximum working time at an applied current of 2A of the coil is 25 minutes.
The coils are driven by the MX100QP S2 programmable power source, with four separate DC power outputs that allow up to 210W from a single output. The power supply's range switching gives variable voltage/current combinations. Each output channel offers selectable ranges of 16V/6A, 35V/3A, and 35V/6A, and has a power supply has a resolution of up to 1mV and 0.1mA.
The Teslameter FM 3002 of the firm Projekt Elektronik GmbH with a one-dimensional Gauss probe is used for magnetic field measurements. For the temperature measurements, a 10$k\Omega$ Negative Temperature Coefficient (NTC) resistance of the firm Farnell was used, placed upon the Helmholtz coils with heat resistant tape and connected to a digital multimeter capable of 4-wire measurements.

3.2. Characterising resistance increase during coil heating

When a constant voltage is applied to the coil, the temperature of the windings rises, as does the resistance of the wire. This reduces the current flowing through the coil, weakening the magnetic field it produces over time. To quantify the resistance change over time, a constant voltage is applied to each coil for 25 minutes, as this is the maximum time the coils can be turned on before they need to be cooled down. The coil resistance is given in Equation 3.1, where I is the current through and V the voltage over the coil. The percentage increase of the resistance can be calculated using Equation 3.2, where R_{start} is the coil resistance at the start of the measurements and R_{end} the resistance at the end.

$$R_{coil} = \frac{V}{I} \tag{3.1}$$

$$\text{Percentage increase} = \frac{R_{end} - R_{start}}{R_{start}} \cdot 100\% \tag{3.2}$$

During this experiment the voltage, current, and temperature of the coils is recorded every minute. The voltage and current are read from the power supply and the temperature is measured by using an NTC connected to a digital multimeter. These measurements are performed for each coil, at intermediate voltage levels corresponding to a magnetic field of roughly $5mT$. At higher voltages, heating and resistance change will be larger, while at lower voltages this will be smaller. This midrange value was selected to get an approximate idea of how resistance changes under normal use, as it is approximately the midpoint of the coils working range. The resistance change over time and temperature can be demonstrated in various ways. Resistance change as a function of temperature can be plotted, demonstrating the underlying physical principles. But more useful for operational characterisation is a resistance vs time plot, which quantifies how resistance changes during operation. Both of these plots for the three separate coils are depicted in Figure 3.1.

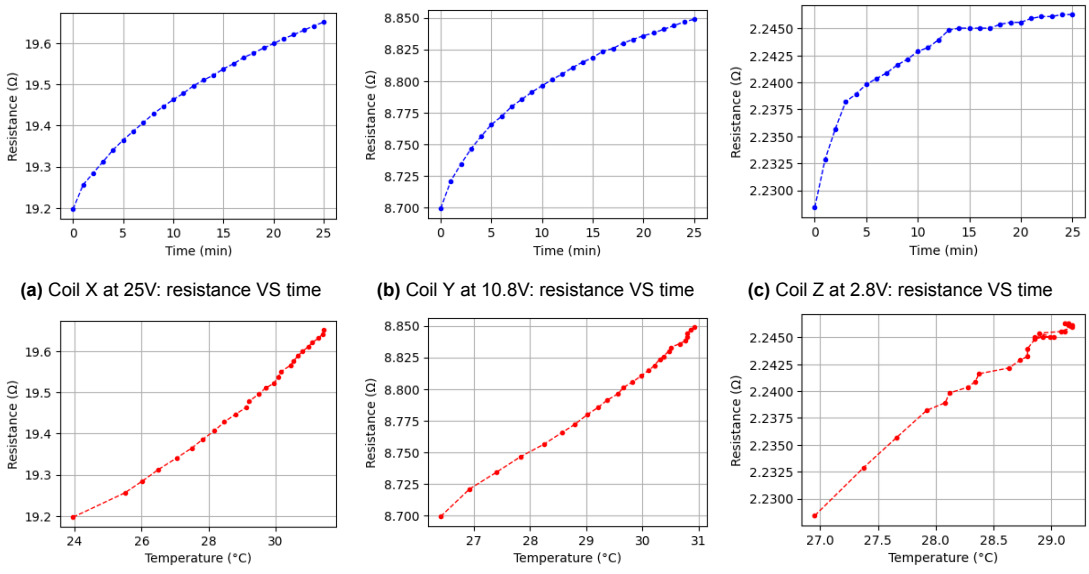

(a) Coil X at 25V: resistance VS time

(b) Coil Y at 10.8V: resistance VS time

(c) Coil Z at 2.8V: resistance VS time

(d) Coil X at 25V: resistance VS temperature

(e) Coil Y at 10.8V: temperature VS resistance

(f) Coil Z at 2.8V: resistance VS temperature

Figure 3.1: Coil resistance plots

Resistance should increase roughly linearly as a function of temperature [10]. This is the case for coils z and y, where the coils handle lower voltages. However, for coil x, which operates at significantly higher voltages, the resistance increases quadratically. There seems to be more internal heating of the coil. Not only is the change of resistance for the z coils relatively small, there is also some stagnation in its increase. At some point, both the resistance and temperature barely change as time increases. This is most likely because of the lower power the z coils dissipate. Over 25 minutes the resistance increases with 2.366% for coil x, 1.721% for coil y, and 0.802% for coil z. These levels of inaccuracy, combined with the variations in the ambient magnetic field, will result in measurements that lie well above the acceptable error of 2% as defined in the Programme of Requirements. Thus, it was decided to control the coils by setting the current, rather than setting the voltage. This way, the current remains constant and, by extension, the magnetic field remains constant as well.

However, the power source that is used in this project cannot directly drive a current, it can merely set a current limit. The power supply operates in constant current mode automatically when the load tries to draw more current than the set maximal current value. So, to apply current control, a current

limit value is set at a load that would otherwise draw more than that current. The current will therefore remain constant, and the heating effects will cause the voltage to rise, instead of the current to drop. The voltage limit is set to 35V, 16V or 5V for the x, y and z coils respectively. These are the voltage values at which the highest magnetic field is created. This approach maintains the desired current, though at the cost of a rising voltage, and thus a rising power output. Since the coils continue to heat up, the 25 minute time limit should still be respected. Nevertheless, this approach ensures a reliable way of creating a constant field.

3.3. Current to magnetic field relationship

The relationship between the applied current and generated magnetic field for each of the 3 axes is the main deliverable of the calibration of the Helmholtz coil. These relationships will be used in the LabVIEW 3D sweeping script. This section discusses the calibration procedure and setup in subsection 3.3.1, and talks through the results in subsection 3.3.2.

It is important to note that the earth's magnetic field and other ambient magnetic field fluctuations in the coils vicinity superimpose on the magnetic field generated by the 3D Helmholtz coil. During preliminary testing it was observed that the magnetic field intensity fluctuates between 0 - 50 μT. This is but a small fraction of the maximal magnetic field produced by the 3D Helmholtz coil, where it does not heavily influence measurements. However, at lower magnetic field strength the ambient magnetic field heavily interferes with measurements. Given a maximum ambient magnetic field of 50 μT and an accuracy requirement of 2 %, measurements should start around 2.5 mT. In Appendix C, the use of the Helmholtz coils below this threshold value of 2.5 mT is discussed.

Even when the Gauss probe is securely placed and does not move, the ambient field fluctuates by approximately ±2 μT at all times. This is intrinsic to the environmental magnetic field, and is considered as external noise rather than system instability.

3.3.1. Measurement setup and procedure

First, the probe is placed in the uniform centre of the coils, and oriented to measure the magnetic field in one specific direction. Instead of locating the correct orientation of the probe by finding where the magnitude of the field in the direction being measured is the strongest, it is found by placing the probe at the height and angle where the magnetic fields in other directions produce the least measurable response. This is a useful method, as it is easier finding a 0, which occurs in a range where a slight change in orientation has a relatively big impact, than finding a maximum occurring in a range where the same minor change also changes the output only slightly.
The probe is taped to a wooden stick, held by a clamp, as depicted in Figure 3.2. This provides a sturdy position for probe, as it is vital that it is not moved after it has been set to its measurement position for the duration of all measurements of one coil to ensure consistency of measurement results. Lastly, to reduce interference caused by ambient fluctuations, the Helmholtz coil should be placed as far from power cables and the power supply as possible.

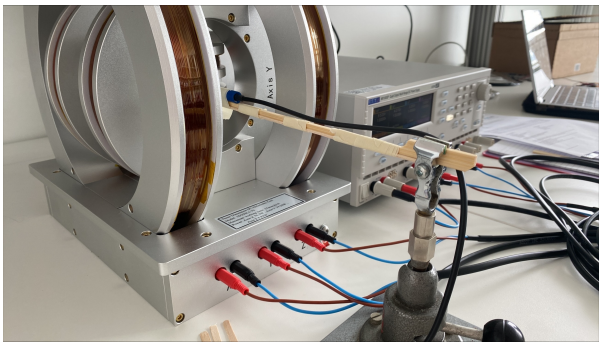

Figure 3.2: Setup of the Gauss meter probe in the 3D Helmholtz coil

Measurements were taken in two opposite directions for each coil axis, where each axis is tested independently from the others [11]. A step size of 0.25 mT was chosen, starting from 2.5 mT, as

mentioned before. This should be enough to catch non-linearities and fit a good calibration curve. Some preliminary measurements based on trial and error were done to find what current step is needed to get this increment in magnetic field.
To increase accuracy and reduce the effect of random errors each measurement is repeated at least 3 times. More measurements are to be taken if operational factors have affected the meter output, or the standard deviation between measurements exceeds 4%.

To start the calibration for a single coil, the probe is positioned as described earlier. A spreadsheet is prepared in advance, listing the target current values, along with columns to record the actual current, voltage, and measured magnetic field. The desired current is set manually on the power supply, with the constant voltage limits of $35V$, $16V$ or $5V$ for the x, y and z coils respectively, to adhere to the limitations as mentioned in section 3.2. For each axis, this is done 3 times for both positive and negative field directions.

3.3.2. Results

For each separate measurement sequence, a line can be fitted through the data points. This results in 3 equations per direction and coil. Firstly, an average is taken of the current to magnetic field relationship per coil. Table 3.1 depicts the resulting relationships for each coil and field direction.

Field	Test	X axis	Y axis	Z axis
Positive	Test 1	3880.8 I + 28.25	4115 I – 12.411	4040.3 I – 61.25
	Test 2	3847.6 I + 32.435	4117.2 I – 12.35	4040.1 I – 60.799
	Test 3	3902.1 I + 15.583	4114.9 I – 12.684	4041 I – 62.696
	Average	3867.8 I + 25.42	4115.7 I – 12.48	4040.47 I – 61.58
Negative	Test 1	- 3934.7 I - 10.751	-4111.8 I + 10.703	-4033.6 I – 40.735
	Test 2	- 3913.6 I – 26.709	-4100.7 I – 0.375	-4036 I – 36.456
	Test 3	- 3909.2 I – 35.989	-4109.6 I + 5.0018	-4035.6 I – 37.148
	Average	- 3919.2I - 24.483	-4107.37 I + 5.11	-4035.07 I – 38.113

Table 3.1: Calibration measurement results per coil for both positive and negative fields. I represents the current in A, and the magnetic field is provided in μT.

It may be observed that for each coil, the positive and negative averaged magnetic field expressions differ slightly. This is due to the presence of a relatively constant ambient magnetic field during both measurement directions. For one polarity the ambient field is added to the coil's field, while for the other it is subtracted. These effects depend on the orientation of the Helmholtz coil within the room during measurements. However, since the coil system can be used at different times and in different settings, where the ambient magnetic field could vary significantly or even be reversed, this discrepancy must be addressed. To minimise the influence of ambient field variation, the expressions for the positive and negative directions were averaged. This results in a single equation per axis. The standard deviations of each coils slope were computed in Appendix B. The standard deviation of each coils slope varies significantly between the coils: the X coil has a standard deviation of 27.59μT, the Y coil 3.23μT, and the Z coil 5.26μT. This corresponds with a relative standard deviation of 0.71 %, 0.08 %, and 0.13 % respectively. These uncertainties lie within the acceptable range. It is clear that the X coil displays higher variations. This likely due to the fact that the X coil has a significantly larger diameter than the other coils, as noted in section 3.2.

All equations derived from the test results are in the form $y = ax + c$. Ideally, when no current is applied, there should be no magnetic field either within the coils, in other words, $c = 0$. However, because of the ever-present background field in the measurements, this is certainly not the case. The intercept c is thus a measure of the average amount of background magnetic field present during the calibration measurements, which is highly dependent on the placement of the Helmholtz coil in the room. The slope dictates the actual relationship between the magnetic field and the current. Therefore, the intercept can be removed, and the slope a is assumed to be the ideal current to magnetic field conversion factor. Thus the dependency on the coil's placement is removed. It is important to keep in mind that when using the Helmholtz coil, the measured field will surely still differ from the obtained relationship, due to the effects of the ambient field and other possible disruptions. Section 3.5 shall continue on this subject.

Thus, the final magnetic field to current relationships are obtained, which are depicted in Table 3.2. These are the conversion factors that shall be used in the LabVIEW script to find the current to be applied to create the desired magnetic field.

X axis	Y axis	Z axis
$B = 3898.0 \cdot I$	$B = 4111.5 \cdot I$	$B = 4037.8 \cdot I$

Table 3.2: Averaged current to magnetic field relationship per axis. With current I in A, the magnetic field is calculated in μT

3.4. Uniformity analysis

This section discusses the coil's uniform sphere, as a uniform field is crucial for reliable measurements. The manufacturer of the Helmholtz coil (Xiamen) has provided specifications on the uniformity within a $2cm$ diameter sphere at the centre of the coil system. This uniformity is validated using the same Gauss probe as used during calibration, and with two commercial sensors. The sensors used are from the companies Melexis and Texas Instruments.

The Gauss probe is placed inside the coils in the same manner as in subsection 3.3.1, and the measured value in the centre is recorded. The probe is then carefully moved $1cm$ to either side, and the measured value is recorded. These values are used to calculate the deviation from the central measurement, quantifying the field uniformity error. This process is performed three times, and the average error is found for each direction. Note that no results are available for the Z coil, as it was incredibly difficult to acquire reliable data with the Gauss probe. The probe setups orientation of the probe is very sensitive to movement, and the available space for adjustments is very limited. Due to the geometry of the z coil (it being the smallest of the coils) any attempt to move the probe resulted in an unintended change in its orientation. The results are depicted in Table 3.3.

The same procedure was performed with the two sensors, the results of which are also depicted in Table 3.3. Note that due to the supports the sensors are mounted upon, the sensors are not able to move the full $1cm$ within the coils. Instead, measurements for the sensors are done with a displacement of approximately 6–7mm in either direction. When comparing the results obtained by the Gauss probe and the sensors, it is observed that the sensors measure a much smaller errors. This is in part due to the reduced displacement distance. Moreover, the Gauss probe setup is more susceptible to errors due to manual adjustment of the probe, which could contribute to a larger error.

Comparing the measured uniformity to the uniformity specifications provided by the manufacturer, it is observed that the error with the Gauss probe is substantially larger than these results as well. This is likely due to the susceptibility of the Gauss probe to errors in its displacement. But, since the sensors were not moved to the edge of the uniform sphere, it would be expected that the errors found are smaller than those of Xiamen. This is not the case for the x and z axes, this could be due to imperfect initial placement and alignment of the sensors.

Aside from this, it can be concluded that the central $2cm$ diameter region of the coils has a high uniformity, exceeding 99% (i.e. less than 1%). However, the sensors placed in the centre of the 3D Helmholtz coil system occupy a significantly smaller volume than this region, and the magnetic field within this smaller area will be even more uniform. Moreover, these uniformity errors are considerably smaller than potential sensor misalignment errors. In this thesis, the field within the sensing volume is assumed to be uniform. This assumption is considered valid based on the demonstrated uniformity of the larger central region.

Coils	Error with Gauss probe (%)	Error with sensors (%)	Xiamen (%)
x	0.57	0.084	0.02
y	0.29	0.068	0.08
z	-	0.55	0.45

Table 3.3: Maximum errors resulting from uniformity measurements with the Gauss probe and the 3D Hall sensors

3.5. Conclusion on magnetic field accuracy and stability

Three main contributors to uncertainty in the generated magnetic field have been identified: ambient magnetic field offset, relative slope variability of each coil, and current-induced magnetic field fluctuations.

The ambient magnetic field was removed during calibration by removing the intercept, but it still influences the absolute magnetic field magnitude during operation. The ambient field can reach up to 50μT, which corresponds to a 2% error at 2.5mT and a 1% error at 5mT. Additionally, the ambient field fluctuates consistently by ±2μT, which limits the stability of the magnetic field. Variability in the current-to-field slope arise from slight differences in coil geometry. The standard deviation of each coil are 27.59μT for the X coil, 3.23μT for the Y coil, and 5.26μT for the Z coil. Lastly, the power supply current fluctuation of 0.1mA results in a total magnetic field uncertainty of 1.20μT across all axes, or 0.048% at 2.5mT and 0.024% at 5.0mT.

Combining these independent uncertainty sources using the root-sum-square method results in the worst-case total uncertainty, which is calculated using Equation 3.3. At a magnetic field strength of 2.5 mT this results in a total maximal uncertainty of 2.298%, as depicted in Equation 3.4. Working backwards, 2.87 mT is found to be the magnetic field strength with a maximal uncertainty of 2%, as shown in Equation 3.5. Note that this does not include the consistent ±2 μT fluctuations from the ambient field, as they are considered as external noise.

$$\begin{aligned}\text{Uncertainty}_{max} &= \sqrt{(\text{uncertainty ambient field})^2 + (\text{uncertainty coil variability})^2 + (\text{uncertainty current fluctuation})^2} \\ &= \sqrt{\left(\frac{\text{ambient field fluctuations}}{B}\right)^2 + \left(\frac{\text{coil variability}}{B}\right)^2 + \left(\frac{\text{current fluctuations}}{B}\right)^2}\end{aligned} \tag{3.3}$$

$$\begin{aligned}\text{Max uncertainty at 2.5 } mT &= \sqrt{\left(\frac{50\mu T}{2500\mu T}\right)^2 + \left((\frac{27.59\mu T}{2500\mu T})^2 + (\frac{3.23\mu T}{2500\mu T})^2 + (\frac{5.26\mu T}{2500\mu T})^2\right) + \left(\frac{1.2\mu T}{2500\mu T}\right)^2} \\ &= 2.298\%\end{aligned} \tag{3.4}$$

$$\begin{aligned}\text{Max uncertainty at 2.87 } mT &= \sqrt{\left(\frac{50\mu T}{2870\mu T}\right)^2 + \left((\frac{27.59\mu T}{2870\mu T})^2 + (\frac{3.23\mu T}{2870\mu T})^2 + (\frac{5.26\mu T}{2870\mu T})^2\right) + \left(\frac{1.2\mu T}{2870\mu T}\right)^2} \\ &= 2\%\end{aligned} \tag{3.5}$$

To conclude, the magnetic field accuracy has a maximal uncertainty of 2.3 % at 2.5 mT. At higher field strengths this decreases, because the ambient field contribution becomes a smaller fraction of the total. 2.87 mT is the field strength at which the combined relative uncertainty from ambient field, coil variability, and current fluctuation is exactly 2 %. It is important to note that this is maximal uncertainty. Most of the time ambient field fluctuations are lower than 50μT, so the actual error is lower. Lastly, the field stability is mainly determined by the power supply current fluctuations, which result in a 1.2 μT fluctuation, which lies within the ±1 μT field stability requirement over 30 minutes.

4

Development of a LabVIEW script for automated 3D field sweeping

This chapter discusses the automated 3D magnetic field sweeping script. Figure 4.1 depicts the setup. It consists of the 3D Helmholtz coil, which is connected to the power supply with banana connectors. The power supply communicates with the LabVIEW script on the computer through serial communication over USB.

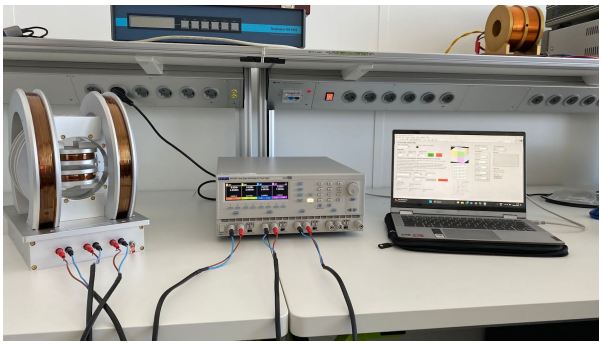

Figure 4.1: 3D magnetic field sweeping setup

Section 4.1 discusses the fundamentals of thee field sweeping logic, and discusses the mathematical framework used to calculate the magnetic field vector's orientation. Next, section 4.2 discusses why LabVIEW was chosen to develop the script, and its working principles. Section 4.3 describes the Graphical User Interface (GUI) that was developed for this script, while section 4.4 covers the developed code structure. Lastly, section 4.5 describes the tests performed to validate the functionality of the script.

4.1. Working principle

4.1.1. 1D magnitude sweep

3D Hall sensor sensitivity measurements consist of applying varying magnetic field strengths separately across each of the three spatial directions (x, y, z). This process can be automated by implementing a magnitude sweep of a 1D magnetic field vector. So, during a 1D magnitude sweep, the magnitude of a magnetic field vector along one axis is varied over a specific range (eg. 3 to 5mT). An example is depicted in figure 4.2, where the magnitude of the unit vector $\hat{x}$ is incremented each step.

First, the sweep range, defined by the minimal and maximal magnetic field strength, and the number of steps should be defined. Equation 4.1 computes increment in magnetic field strength between each

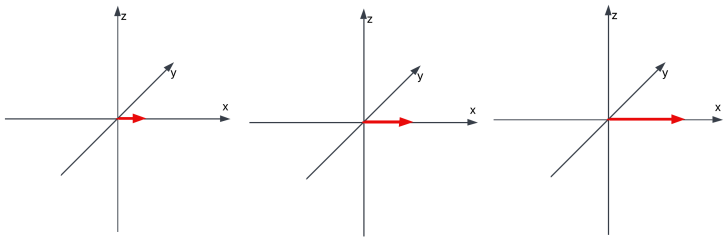

(a) Step 1 of the 1D magnitude sweep **(b)** Step 2 of the 1D magnitude sweep **(c)** Step 3 of the 1D magnitude sweep

Figure 4.2: Visual representation of the 1D magnitude sweep

step. Then, equation 4.2 gives the magnetic field strength at each step *i*. These equations define how the magnetic field strength is increased throughout the sweep.

$$B_{\text{increment}} = \frac{B_{\text{max}} - B_{\text{min}}}{\text{number of steps}} \tag{4.1}$$

$$B_{\text{step i}} = B_{\text{min}} + i \cdot B_{\text{increment}} \tag{4.2}$$

4.1.2. 3D magnetic field sweep

Basics of the 3D magnetic field sweep

The magnetic field sweep is a constant-magnitude, fixed-tilt, azimuthal sweep of a 3D vector. This results in a trajectory where two of the vector components change sinusoidally and the third component remains constant. The total field vector magnitude remains constant throughout the sweep. Throughout the sweep the vector tip traces out a circle in the sweeping plane, eventually tracing out a full cone. This approach builds upon a 2D sweep that was created in preparation for the 3D sweep, where the vector traced a circle in a 2D plane. Moreover, this sweep fulfils the requirement to have a magnetic field with 3 components, sweeping through the 3D space.

Figure 4.3 is a visual representation of a sweep of one octant, namely octant III. The numbering of the respective octants is depicted in Figure 4.4. The red arrow represents the magnetic field vector, with a constant magnitude chosen by the user. The user has further defined the fixed axis and the angle θ with this axis. The fixed axis is the name for the axis along which the component of the magnetic field does not change for the duration of the sweep, the other two axes form the sweeping plane. The user can then decide how many steps to take per sweep, resulting in a certain increment in the angle ϕ, calculated by dividing 90°by the number of steps. In the presented example, the z axis is chosen as the fixed axis with a resolution of 3 steps. Figure 4.3a shows the initial conditions when the programme is started, defined as step 0. When the user clicks the button to proceed to the next iteration, the state shown in Figure 4.3b appears, where the angle ϕ can now be seen. After two more clicks during which ϕ is incremented, the last step, as depicted in Figure 4.3d, is reached. In general, there is consistency in the way the cone is traced out. Looking from the origin to the circle that is created in the sweeping axis, this is always done clockwise. This decision has been made for consistency in operation and coding of the 3D sweep.

This example demonstrated a sweep through only one octant. A full magnetic field sweep is supposed to trace out an entire cone in 3 dimensional space. However, a limiting factor is that the power supply can only deliver positive currents and voltages. It is therefore unable to produce magnetic fields that require a negative current, that is to say, negative magnetic fields. If a field in the opposite direction is required, a physical polarity switch is necessary. This is done by reconnecting the cables the other way around. For this reason, one execution of the script sweeps through one octant of the Cartesian 3D space. The cables can then be reconnected accordingly, and the script can be run again. The table depicted in Figure 4.5 tells the user how to connect the cables for each specific octant. For a full sweep, the code must thus be run four times, with a cable polarity switch between each octant.

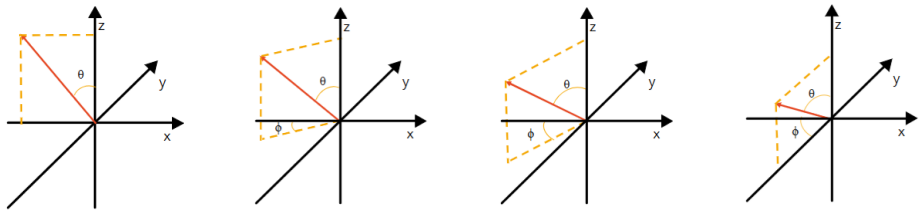

(a) Step 0 of the 3D field sweep

(b) Step 1 of the 3D field sweep

(c) Step 2 of the 3D field sweep

(d) Step 3 of the 3D field sweep

Figure 4.3: Visual representation of the 3D magnetic field sweep through one octant, taking 3 steps

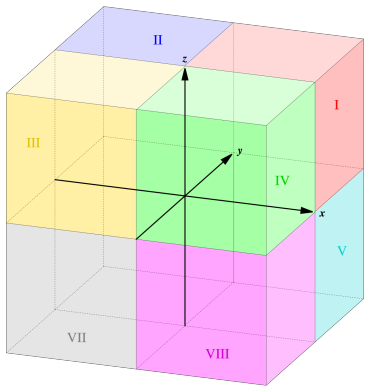

Figure 4.4: Octant numbers [12]

Mathematical framework

All Cartesian axes should be able to act as the fixed axis for the 3D sweep. The calculations for the fixed axis and sweeping plane are always the same. Therefore, a generalized approach is taken for the calculations of the 3 components of the magnetic field. The magnetic field vector components are first calculated in a hypothetical coordinate system defined by three axes: A, B and C. A and B define the sweeping plane, while C represents the fixed axis. This method allows the same set of equations to be reused for any axis configuration. Equations 4.3, 4.4 and 4.5 depict the goniometric formulas used to calculate the magnitude of the vector components. B_{total} is the constant magnetic field magnitude as defined by the user, and the angles ϕ and θ are the angles as discussed in subsection 4.1.2. As C remains constant throughout the entire sweep, it only needs to be calculated once at the beginning. ϕ is incremented each iteration, so A and B do need to be recalculated for each step.

$$A = B_{total} \cdot cos(\phi) sin(\theta) \tag{4.3}$$

$$B = B_{total} \cdot sin(\phi) sin(\theta) \tag{4.4}$$

$$C = B_{total} \cdot cos(\theta) \tag{4.5}$$

By using these three hypothetical axes, the three components can easily be calculated, after which the values only need to be passed on to the correct Cartesian direction, based on the user input. Table 4.1 is the lookup table used for the mapping of the axes A, B and C to x, y and z. Note that multiple octants require the same connection between the hypothetical and physical axes. This makes the integration of these highly repeatable operations into the LabVIEW script easier.

Sweeping plane	Octants	A	B	C
xy	$I, III, VI, VIII$	x	y	z
	II, IV, V, VII	y	x	z
xz	II, IV, V, VII	x	z	y
	$I, III, VI, VIII$	z	x	y
yz	$I, II, VII, VIII$	y	z	x
	III, IV, V, VI	z	y	x

Table 4.1: Lookup table: connection A, B, C with respective axes

4.2. LabVIEW environment

LabVIEW is a graphical programming environment developed by National Instruments. Instead of text-based code it uses visual block diagrams consisting of icons and wires, which is easier to use for scripts where hardware interaction is needed. LabVIEW programs are called Virtual Instruments (VI), which consist of a front panel, which displays the graphical user interface, and a block diagram, which contains the code. The script makes use of a large variety of subVI's, which are smaller VI's that can be called from within another VI's block diagram. SubVI's act like functions in other programming languages, they simplify code and enable code to be reused.

It was chosen to use LabVIEW for the script instead of Python or Matlab. This is because LabVIEW offers the ability to create user-friendly graphical user interfaces (GUIs) for instrument control. LabVIEW enables the automation of power supply control tasks, such as setting specific output values, and it can also log data from the power supply. Moreover, many manufacturers provide instrument drivers, which make communication with the power supply simpler, as there is no need to learn the power supply's communication protocol. Drivers include VIs for common power supply functions, such as setting voltage and current values and turning channels on or off. However, there was no working driver available for the Aim-TTi MX100QP programmable power supply, so a new instrument driver had to be developed. The power supply is controlled using LabVIEW's Virtual Instrument System Architecture (VISA), which supports serial communication via USB.

4.3. Graphical User Interface

The script allows three kinds of magnetic field control: a static field , 1D magnitude sweep, and 3D field sweep. The operating mode can be selected manually, through the GUI in LabVIEW. Figure 4.5 depicts the GUI developed for this script.

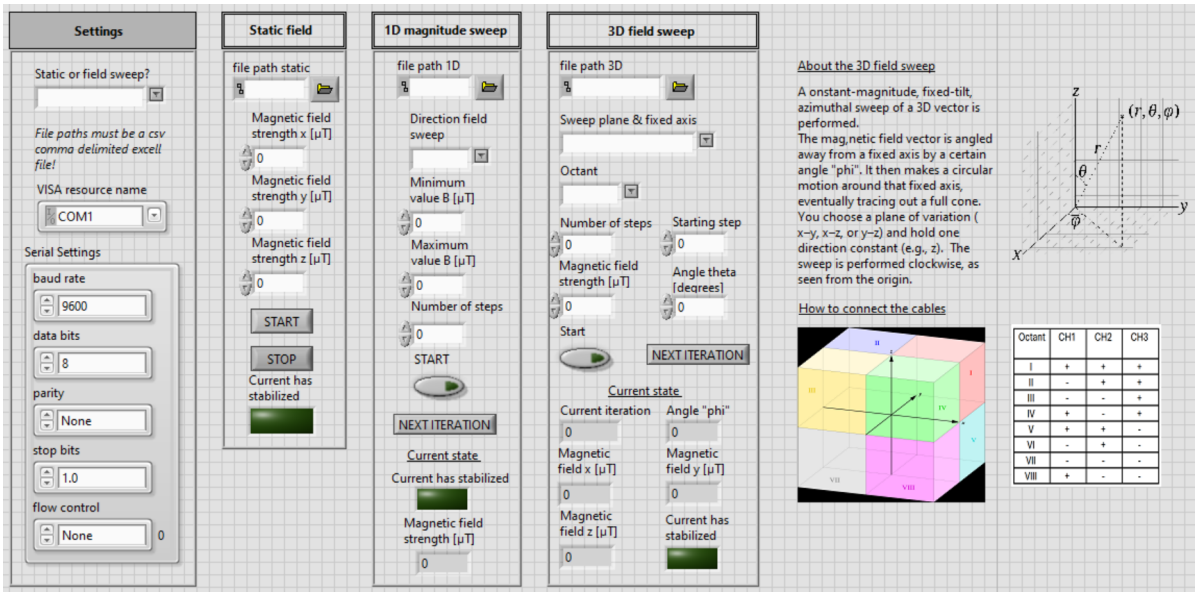

Figure 4.5: Graphical User Interface

In the *settings* section of the GUI there is a mode selector that allows the user to select between the three operating modes. Next, the USB port selector specifies the connection to the power supply, under which the serial settings of the power supply are displayed. Each operation mode also requires the user to select the destination Excel file for data logging.

In static field mode the system generates a magnetic field vector consisting of three vector components: x, y, and z. The user can select individual magnetic field strength along the x, y, and z directions. There are also two buttons, start and stop, which allow the power supply to be switched on and off. Next to that there is also a light that switches on when the current flowing through the coils has stabilized. The reasoning behind this is explained in section 4.4.

In 1D magnitude sweep mode the system performs a sweep, as discussed in subsection 4.1.1.
The GUI consists of multiple controls for the 3D field sweep, namely:

- Direction field sweep: The user must select the direction of the magnetic field vector (x, y, z).
- Minimum value: The user selects the start value of the sweep.
- Maximum value: The user selects the final value of the sweep.
- Number of steps: The user must specify the number of steps taken during the sweep.

To start the sweep, the ”start” button must be pressed, and each step is advanced by the user with a ”next iteration” button press. Under the ”current state” title the GUI displays the actual field value, and a light that switches on when the current flowing through the coils has stabilized.

In 3D field sweep mode the system performs a sweep, as discussed in subsection 4.1.2.
The GUI consists of multiple controls for the 3D field sweep, namely:

- Sweep plane and fixed axis: The user must select the sweep plane and fixed axis, of which the choices are: x-y plane (z held constant), x-z plane (y held constant), and y-z plane (x held constant).
- Octant selection: The user selects the octant in which the sweep is to be performed, which ranges from I-VIII.
- Magnetic field strength: The user must specify the constant magnetic field strength that is held during the sweep in T.
- Fixed angle θ: The user must specify the angle θ, which is measured from the held axis, to determine the orientation of the sweep vector within the plane.
- Sweep resolution *N*:V The user must specify the number of steps taken during the sweep.
- Starting step: The user can specify at which step number to begin the field sweep, rather than only being able to start from the beginning.

To start the sweep, the ”start” button must be pressed, and each step is advanced by the user with a ”next iteration” button press. Under the ”current state” title the GUI displays the actual field values, which include the current iteration, azimuthal angle ϕ, the magnetic field strength in each direction, and a light that switches on when the current flowing through the coils has stabilized.

To the right of the selectors, several figures are provided to guide the user. There is a figure illustrating the definition and numbering of octants used in the sweep, a schematic explaining how to connect the power supply cables for each corresponding octant, and a figure depicting the orientation of the azimuthal angle ϕ and θ within the sweep plane.

At the end of the sweep, the logged Excel file contains entries recorded approximately every 10 seconds. The log includes:

- Static field mode: a timestamp, and the coil voltage, current, and generated magnetic field strength in all three directions (x, y, z).
- 1D magnitude sweep mode: the iteration number, a timestamp, the direction of the field sweep (x, y, z), and that coils voltage, current, and generated magnetic field strength.
- 3D magnetic field sweep: the iteration number, a timestamp, angle θ, angle ϕ, and the coil voltage, current, and generated magnetic field strength in all three directions (x, y, z).

4.4. Code structure

4.4.1. Overview

The developed script is provided in Appendix D. Section 4.1 discussed the working principle of the magnetic field sweep script, defining the 1D field sweep as a magnitude sweep and the 3D field sweep as a constant-magnitude, fixed-tilt, azimuthal sweep of a 3D vector. It also presented the the mathematical framework used to calculate the magnetic field vector's orientation at each step. This section builds upon that basis to describe the field sweeping script. Figure 4.6 depicts the block diagram upon which the script is based. As discussed in section 4.3 the script has three operating modes: static field, 1D magnitude sweep, and 3D field sweep. First, the user must select the operation mode.

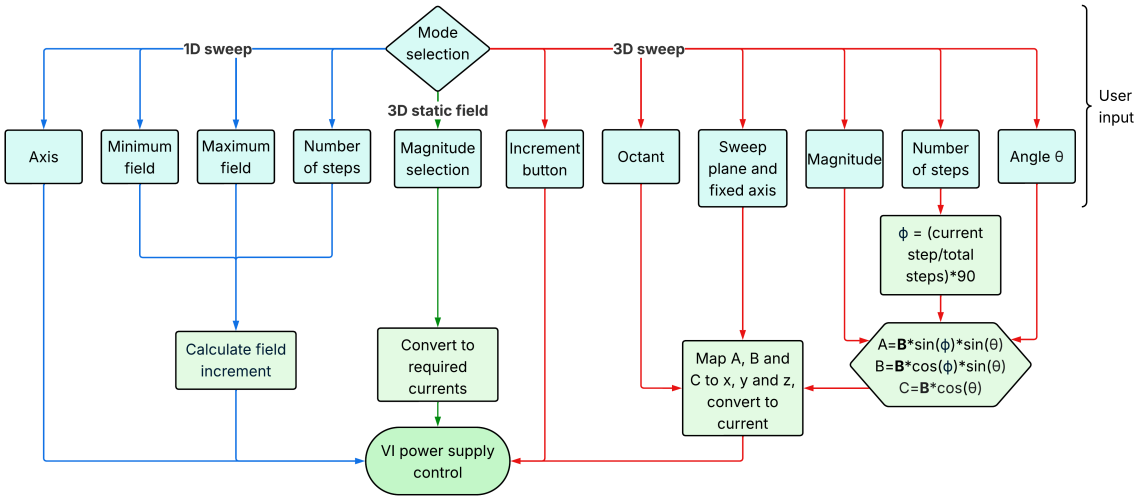

Figure 4.6: Block diagram 3D field sweep

In static field mode, the structure is simple. The code calculates the required current values for each axis using the current-to-magnetic field relationships calibration described in chapter 3. These calculated currents are then sent to the power supply along with the corresponding voltage limits for each channel and the channels are turned on. However, a hardware limitation causes a mismatch between the commanded and actual output currents, where the actual output current is consistently lower by 0.1 to 0.5mA. To compensate this, a closed-loop feedback control mechanism is implemented. After the initial currents are set, the script request the actual current from the power supply, reads it, compares it to the target value, and corrects it if necessary. Lastly, as per functional requirement 1.3, the current system state (which includes the iteration step, timestamp, voltage, current, and magnetic field strength for each coil) must be logged continuously at approximately 10-second intervals. Both the logging and feedback control processes run continuously after the initial current values are sent, until the "stop" button is pressed. At that point, all the channels are turned off.

The operation of both magnetic field sweeps is more complex. Each iteration, new magnetic field values need to be applied in the coil, as described in section 4.1. These values are dependent on the the user-defined inputs. So each iteration new current values need to be calculated and sent to the power supply. Additionally, in the first iteration voltage limits need to be applied and the channels need to be switched on. At the end of the sweep, the channels must be turned off.
The same hardware limitation as mentioned earlier takes place, affecting the accuracy of the generated magnetic field. To compensate this, the same type of logging and closed-loop feedback control processes run continuously after the new current values are sent, until the "next iteration" button is pressed. At that point, new current values are sent again, and the logging and correction cycle restarts.

The LabVIEW script is encircled by a while loop, which runs continuously to ensure that the program stays running the whole time, and the user does not have to restart the program when starting another session. Inside this while loop there is a case structure to switch between the three operating modes: static field, 1D magnitude sweep, or 3D field sweep mode. Each mode has a different logic and field

control behaviour, but they do share a range subVI's that perform common functions. To clearly explain the functionality of the code, subsection 4.4.2 begins by describing the communication method with the power supply. Subsection 4.4.3 discusses each subVI's functionality and purpose, starting with the simplest and building up to the more complex subVI's. Finally, in subsection 4.4.4, the use of these subVI's within the operating modes is explained, providing a complete overview of the script's behaviour.

4.4.2. VISA communication

Communication with the power supply is handled via VISA functions. A VISA application goes through a series of steps, as shown in Figure 4.7. First, the session to a given VISA resource, which is selected on the GUI, is opened. The communication settings dictated by the power supply's manual are configured (baud rates, data bits, parity bits, stop bits, flow control). Then a command is sent to the device using the VISA write function, where the commands are constructed as strings. Next, a specified number of bytes is read from the device. At the end the session to the resource is closed, and any errors that may have occurred are handled. The structure and formatting of the commands are discussed in chapter 12 of the MX100QP Power Supply Instruction Manual [13].

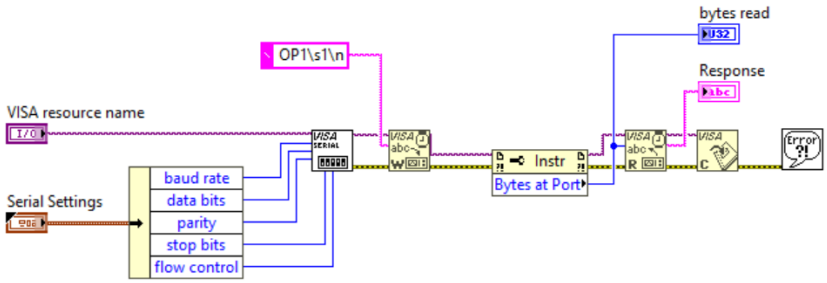

Figure 4.7: VISA application example

Multiple instructions can be combined in one single string and sent to the power supply using a single VISA Write function. However, a limitation of the device is that only one response can be returned per VISA Read session. If multiple instructions that each expect a response are sent in a single session, the reply received via VISA Read is incorrect. Therefore, any command that expects a response must be sent individually, directly followed by a separate VISA Read.

In the finalised script, the opening of the VISA resource session and configuration of communication settings are performed at the beginning of the script, outside the mode selection case structure. The VISA Write and VISA Read operations are performed in the case statement, often incorporated into subVI's and loops. Finally, the VISA session is closed, also outside of the mode selection case statement.

4.4.3. SubVI's

To ensure simplicity and clarity in the code, a range of subVI's were created. These help simplify complex block diagrams by breaking down code into smaller units. These subVI's range from communication with the power supply, to physical calculations and magnetic field sweep management. Table 4.2 provides an overview of the developed subVIs and their purposes. A more detailed explanation of each subVI's functionality is presented in appendix E.

Type	SubVI	Purpose	Inputs	Outputs	Dependencies
Power supply communication	Current control	Three separate subVI's that set the current limit for CH1, CH2, and CH3.	Current to be set (in A)	Command string	Called by static/sweep instruction generators.
	Voltage control	Set the voltage limits for all channels.	\	Command string	Called by static/sweep instruction generators.
	Channel control	Turn all channels on.	\	Command string	Called by static/sweep instruction generators.
		Turn all channels of.	\	Command string	Called by static/sweep instruction generators.
	Query voltage	Three separate subVI's that query the actual voltage on CH1, CH2, and CH3.	\	Command string	Called by the current feedback control mechanism.
	Query current	Three separate subVI's that query the actual current on CH1, CH2, and CH3.	\	Command string	Called by the current feedback control mechanism.
Maths: magnetic field ↔ current conversion	Magnetic field-to-current conversion	Three separate subVI's that convert the magnetic field to current for each axis.	Desired B-field (µT)	Coil current (A)	Called by static/sweep instruction generators & for feedback and display purposes.
	Current-to-magnetic field conversion	Three separate subVI's that convert the current to required magnetic field for each axis.	Coil current (A)	Magnetic field strength (µT)	Called by static/sweep instruction generators.
Maths: 1D sweep step calculation	1D sweep step calculator	Calculates current for selected coil at each step.	Maximal current, minimal current, number of steps, current iteration.	Current at iteration i	Used by 1D sweep instruction generator.
Maths: 3D sweep step calculation	3D A and B	Calculates the in-plane components of the vector each step.	Fixed field strength (µT), θ, total steps N, current iteration n	Magnitudes A and B	Used by sweep instruction generator.
	3D C	Calculates the fixed-axis component of the vector each step.	Fixed field strength (µT), θ, total steps N	Magnitude C	Used by sweep instruction generator.
Maths: current correction	Correct current	Calculates the corrected current value to be sent to the PS.	Measured coil current I_{actual}, desired coil current $I_{\text{necessary}}$, previously set current I_{set}	Corrected coil current $I_{\text{set, new}}$	Used by current correction mechanism.
Instruction control	Static field instruction generator	Generates the correct instructions to be sent to the power supply in static field mode by converting magnetic field to coil current and formatting command strings.	Magnetic field vector (x, y, z).	Coil current values (x, y, z), string commands.	Calls magnetic field to current conversion (B→I) & power supply command communication subVI's.
	1D sweep iteration instruction generator	Generates the correct instructions to be sent to the power supply in 1D magnitude sweep mode, at every step.	Minimum B, maximum B, direction of field sweep, current iteration, and number of steps.	String commands, current channels x, y, z, and B of used axis.	Calls magnetic field to current conversion (B→I), power supply command communication subVI's and 1D sweep step calculator.
	3D field sweep iteration instruction generator	Generates the correct instructions to be sent to the power supply, at every step of the sweep	Sweep plane and fixed axis, octant, current iteration, number of steps, magnetic field strength, θ	String commands per step, ϕ, the resulting magnetic field along each axis (x, y, z)	Calls 3D A and B, 3D C, magnetic field to current conversion, power supply command communication subVI's.

Table 4.2: SubVI's and their purpose

4.4.4. Feedback control and logging

All three modes use the same logic to perform continuous data logging and current feedback correction. This code consists of a flat sequence structure and nested loops. However, it has not been encapsulated by a subVI, as the process relies on real-time button presses to advance to the next loop iteration and displays updated values on indicators during the loop. If the controls and indicators were placed outside the loop, its value is read once when the loop starts and not again until the next loop execution. So, moving the loops into a subVI would prevent the process from detecting these button presses in real time. That is why these loops are not modularised, even though it contains reusable logic.

The process is structured using a flat sequence with two frames, which enables the execution of a sequence of operations in a defined order. This was done to ensure that the headers are only written once at the start, as described in section 4.3. The first frame initialises the headers of each column. The data is always logged in the same order: Iteration, Set the time stamp, Voltage X, Current X, Magnetic field X, Voltage Y, Current Y, Magnetic field Y, Voltage Z, Current Z, Magnetic field Z.

The second frame performs continuous data logging and current correction. Since both modes use the same underlying logic, this section will first discuss the static field mode. Then, the field sweep modes are discussed as an expanded version of the same system.

Static field mode

Figure 4.8 depicts the flowchart for this mode, which is activated when the ”on” button is pressed. First, a for loop that iterates 11 times is executed, each time appending a header to a string array. When the for loop has ended, this array is written to the file using using *Write to Spreadsheet File.vi*.

Frame 2 first generates the instructions to be sent to the power supply and the necessary currents for each coil using the *Static field instruction generator* subVI. After this, a while loop is started, which is only exited when the ”stop” button is pressed. The inputs of this loop are the target current values, a string containing the instructions to be sent to the power supply, the VISA resource name, and error clusters. The outputs are the updated VISA resource name and the error cluster (error out). The VISA Write and Read functions are placed inside the loop, because each iteration needs to send and receive a different instruction/response pair. If the VISA commands were outside the loop, only one interaction would occur, which would result in communication errors.

The while loop contains a for loop, which handles the data collection, data logging, and current correction. One row of data is written to the spreadsheet file per while loop iteration.

The while loop utilises 3 shift registers to pass on information throughout iterations: $I_{set,X}$, $I_{set,Y}$, and $I_{set,Z}$, which store the most recent set current for each channel. Similarly, the for loop has it's own shift registers: *actual current X*, *actual current Y*, and *actual current Z*, which store the current measured in that loop cycle.

The for loop performs as follows:

0. Iteration 0: The iteration number *N* is logged. If it is the first iteration of the while loop, the startup instructions are sent to the power supply. Otherwise, the *current has stabilized* light is turned on. A $2s$ wait statement is introduced to ensure that the power supply has enough time to execute all the instructions it has received.
1. Iteration 1: timestamp is logged.
2. Iteration 2-10a: For each coil (X, Y, Z), the following occurs in sequence:
    - Voltage is queried and logged
    - Current is queried, logged, and placed on the corresponding shift register.
    - Magnetic field is calculated (using the *magnetic field to current conversion* subVI and logged.
3. Iteration 10b: In the final iteration, simultaniously with the magnetic field Z logging, the current correction is executed. For each coil:
    - The difference between the necessary current and the target current is calculated and the new current is obtainedn using the *current current* subVI.

- These corrected current is sent to the power supply and placed on the respective shift registers.

Note that a 500 ms wait is introduced between iterations to prevent buffer overload and allow for reliable communication with the power supply. A 3s wait statement is introduced in iteration 9 (request & log current CH3), to ensure a logging interval of approximately 10s, while making sure that the corrected current is measured promptly in the following logging step.

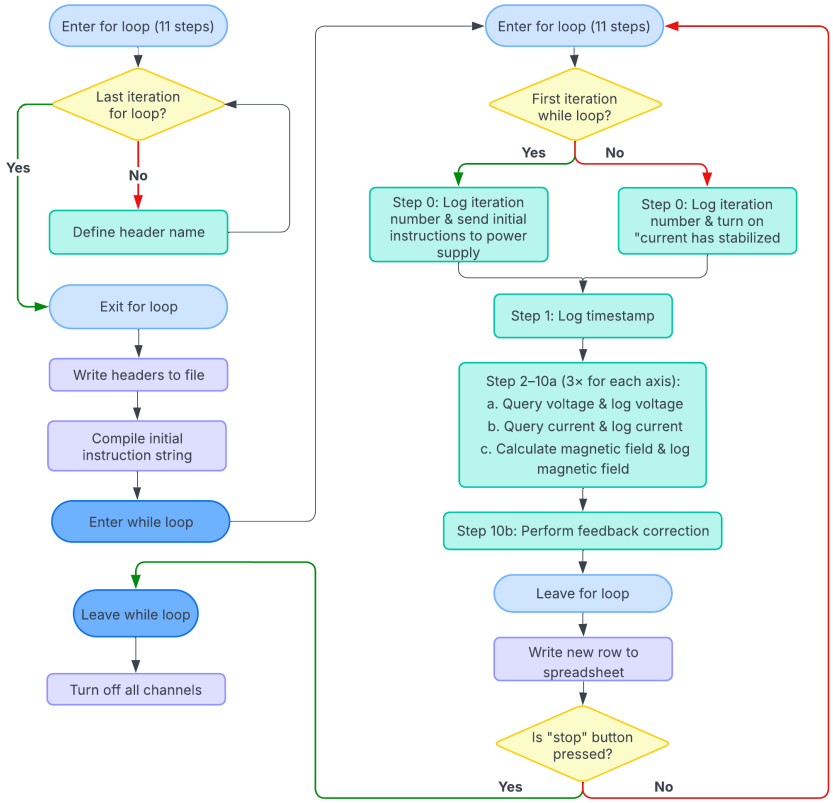

Figure 4.8: Flow chart static field mode

Field sweep mode

In static field mode, the data logging and current correction loop runs continuously until the ”stop” button is pressed. In both the 1D magnitude sweep and the 3D field sweep modes this while loop is encapsulated within an outer for loop, consisting of *N+2* steps, where *N* is the user-defined step size. The extra two steps account for the initial step (step 0) a final step to turn all channels off. Each iteration of this for loop corresponds to a sweep step, and proceeds when the “next iteration” button is pressed. The flowchart of this script is depicted in Figure 4.9.

At the beginning of each sweep iteration the *1D sweep iteration instruction generator* subVI (for the 1D magnitude sweep) and the *3D field sweep iteration instruction generator* subVI (for the 3D field sweep) generate the instructions to be sent to the power supply. These values are converted to their respective currents, and passed on to the inner while loop, the data collection and current correction loop. This while loop functions in exactly the same manner as the one discussed in subsection 4.4.4, and terminates when the ”next iteration” button is pressed. At that point, new current values are calculated and sent to the power supply again, and the logging and correction cycle restarts. This process repeats for each sweep iteration until the final iteration is reached, after which the sweep is finalised.

Note that in 1D magnitude sweep mode the data logging and current correction loop composes of only 6 iterations, and in 3D magnetic field sweep mode it composes of 13 iterations. This is because the 1D sweep generates a magnetic field vector in but one direction. Only one power supply channel is used,

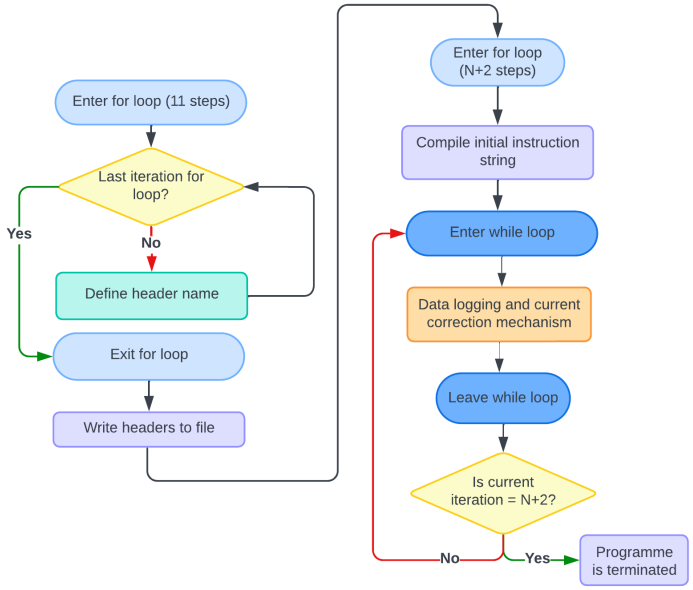

Figure 4.9: Flow chart for both sweep modes

so only one channel's values need to be queried and corrected. While in 3D field sweep mode two extra columns are added, namely angles θ and ϕ. This is reflected in the amount of case statements included in the for loop.

4.5. Testing and validation

The static field and field sweep tests were tested with limited experiments, as only a one-dimensional Gauss probe is available. Full-field validation is performed in the next chapter, where the magnetic field is indirectly assessed via sensor characterisation and sweeping.

Thus, this section is focused on confirming that the control logic executes as intended. More specifically, that the correct currents are calculated and sent to the power supply every iteration, the feedback mechanism measures the actual current and applies appropriate correction, and that the logging to the spreadsheet functions as required. This can be done by observing the power supply screens, which display the actual measured current $I_{measured}$ and the set current values I_{set} of each channel. At each iteration of the field sweep three validation steps were undertaken:

- Applied current: The current values sent to the power supply are calculated and cross-checked with the readings displayed on the power supply's screen.
- Feedback current correction: Comparison of I_{set} and $I_{measured}$ live during operation, to confirm that the code's closed-loop correction algorithm is actively adjusting current outputs when necessary.
- Data logging: After each sweep, the spreadsheet is opened to confirm that the correct number of rows were logged, values were placed in the correct columns, and timestamps and current values matched the expected iteration structure.

Static fields and sweeps were performed under different operating conditions, using a variety of combinations of resolution, octant, field orientation, and angles. In each case it was confirmed that the applied current, feedback current correction, and data logging function as required. A new row of data is appended approximately each 10s, which is in line with the requirements.

An example of a sweep test was performed using the following parameters: x–y sweeping plane, octant V, 3 steps, and an angle θ of 45°. The logged data is shown in Table 4.3. Note that the angle θ and angle ϕ are not included, as to ensure visibility. This example shows that the system functions as intended. The current values sent to the power supply each sweep step are correct, and the current

correction mechanisms functions properly. The logged data file correctly places all information into the appropriate columns. Note that row without entries occur when the ”next iteration” button was pressed.

Iteration	Time stamp	Voltage X (V)	Current X (A)	Magnetic field X (uT)	Voltage Y (V)	Current Y (A)	Magnetic field Y (uT)	Voltage Z (V)	Current Z (A)	Magnetic field Z (uT)
0	13:45:55	-0.021	-0.0012	-4.6776	7.485	0.8596	3534.245	1.952	0.8754	3534.69
0	13:46:05	0.004	0	0	7.49	0.8599	3535.479	1.954	0.8756	3535.498
0	13:46:14	0.004	0	0	7.491	0.8599	3535.479	1.954	0.8756	3535.498
0										
1	13:46:26	8.77	0.4533	1766.963	6.485	0.7445	3061.012	1.954	0.8754	3534.69
1	13:46:35	8.775	0.4535	1767.743	6.487	0.7446	3061.423	1.955	0.8756	3535.498
1	13:46:45	8.776	0.4535	1767.743	6.489	0.7447	3061.834	1.955	0.8756	3535.498
1	13:46:55	8.776	0.4535	1767.743	6.489	0.7447	3061.834	1.955	0.8756	3535.498
1										
2	13:47:06	15.189	0.7853	3061.099	3.746	0.4299	1767.534	1.955	0.8754	3534.69
2	13:47:16	15.195	0.7855	3061.879	3.748	0.43	1767.945	1.956	0.8755	3535.094
2										
3	13:47:27	17.543	0.9066	3533.927	0	0	0	1.956	0.8754	3534.69
3	13:47:37	17.554	0.907	3535.486	0	0	0	1.956	0.8756	3535.498
3										

Table 4.3: Example sweep test: logged data

5

Sensor measurements and validation results

This chapter discusses the characterisation of two commercial 3D Hall effect sensors, followed by the application of a 3D magnetic field sweep to evaluate their response. Moreover, results from some characterisation of the pyramid sensor are presented. The characterisation is discussed in section 5.1, including the measurement setup and the results. In section 5.2, the 3D sweeping script is run and the resulting data of the sensors is analysed, focusing on the errors made. In section 5.3 the calibration results from chapter 3 are compared to the data as provided by the manufacturer of the 3D Helmholtz coil, as well as the results of the sensor characterisation. Lastly, in section 5.4, sensitivity measurements are conducted using the inverted pyramid 3-axis silicon Hall-effect magnetic sensor developed at the TU Delft.

The two commercial Hall sensors used in this chapter are the Texas Instruments TMAG5173A1QDBVRQ1 and the Melexis Technologies MLX90393ELW-ABA-011-SP. They will be denoted by their companies' name from this point onwards. Both chips are a combination of two VHD's with one PHD.

5.1. Sensitivity measurements

In subsection 1.3.1 the concept of sensitivity was briefly introduced. It is the relation between the output voltage and the incident magnetic field, in other words the slope of the output curve of the sensor, from which the unit V/T follows. However, because the sensors provide a digital readout, the output voltage is converted to a defined sequence of bits. The sensitivity is therefore often given in datasheets in a unit resembling LSB/T, where LSB stands for Least Significant Bit. This unit can be interpreted as the minimum change in magnetic field that causes a detectable change in the output. The objective of these sensitivity measurements is to compare those of the two sensors with each other and their specifications, so this unit is adopted from this point onwards.

These measurements and comparisons are performed for future reference, to be able to compare the functionality of the pyramid sensor with those of readily available commercial sensors. Moreover, within this project, the measurements can be used to validate the calibration process, as will be discussed in section 5.3. subsection 5.1.1 presents the measurement setup and procedure, after which the results of the performed measurements are presented and discussed in subsection 5.1.2.

5.1.1. Measurement setup and procedure

As with the calibration measurements setup, the sensitivity measurements are done with the 3D Helmholtz coil connected to the MX100QP power supply. The sensors are read out using an Arduino Nano. The accompanying readout code was provided by the other subgroup of this Bachelor Project. To place the sensors at the correct height, an individual cylindrical support was 3D printed for both sensors. These supports are depicted in Figure 5.1. This was placed inside the Helmholtz coil and oriented correctly. The correct orientation was obtained in a similar manner as described in subsection 3.3.1,

by turning one channel on and minimizing the response of the other two channels. When the appropriate placement was found, the Helmholtz coil and sensor were not moved for the entire duration of the measurements.

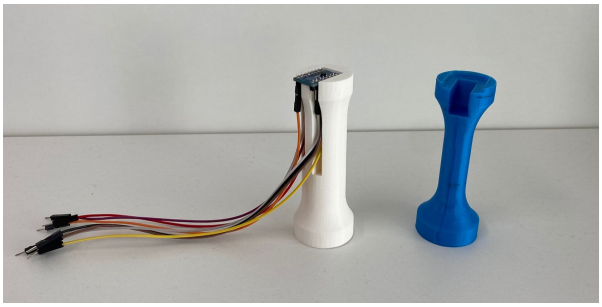

Figure 5.1: 3D printed supports for the sensor sensitivity measurements

Measurements were undertaken for both sensors, where a measurement series consists of 10 measurements from 2.5 to 7mT, taking steps of 0.5mT. The measurement series is repeated 3 times for both the positive and negative fields, for all three axes. The appropriate magnetic field at each measurement point was generated by applying the corresponding current to the power supply. For each measurement point, the voltage and current supplied by the power supply and the sensor readout were recorded. The measurement results of the sensor in all three directions (x, y, z) were recorded, as opposed to only the one corresponding to the axis undergoing measurements. This was done be able to detect any crosstalk or other discrepancies between the three channels.

The sensor readout code displays the measured magnetic field in all three directions. This is useful for validating the calibration of the 3D Helmholtz coil, however, sensitivity measurements require the actual bit sequence values. This can be obtained easily by using the sensitivity provided in the data sheets [14],[15]. For each measurement series, there are now 10 pairs of applied magnetic field and output bit sequence. Similar to the calibration procedure, a linear relationship can be found for this data where the slope is of interest. For the three axes, an average is taken of the slopes of all measurement series, which is the sensitivity of that axis.

5.1.2. Results sensitivity measurements

For both sensors, the procedure as described above results in 3 sensitivities, one for each direction. Table 5.1 shows these results, alongside the values provided in the data sheets, and the error between the measured sensitivity and the manufacturer's. The provided sensitivity of the Melexis sensor was given in the unit $\mu T/LSB$. For ease of comparison and consistency, this has been converted to LSB/mT, which is the unit Texas Instruments uses.

Axis	**Texas Instruments**			**Melexis**		
	Datasheet (LSB/mT)	Measurements (LSB/mT)	Error (%)	Datasheet (LSB/mT)	Measurements (LSB/mT)	Error (%)
x	844	791.33	6.24	4000	4109.92	-2.75
y	844	807.37	4.34	4000	4214.27	-5.36
z	844	857.18	-1.56	2481	2620.58	-5.63

Table 5.1: Results of the sensitivity measurements

The large size of the errors is noticeable. Texas Instruments provides data on the possible error in sensitivity; typically $\pm$0.4% and at most $\pm$2.5% [14]. The measured sensitivity in the z direction falls within this range, but the measured x and y sensitivity errors are much larger. Melexis has not provided such parameters, but the errors of over -5% are very large as well. It is possible that part of the size of these errors come from inaccuracies in the calibration of the Helmholtz coil, whose calibration results were used to drive the coils during these measurements. Moreover, even though great care was taken to ensure good placement of the sensors, this could be another source of error.

Comparing the two sensors with each other, two observations can be made. First of all, the Melexis sensor has much larger sensitivity than the Texas Instruments. A larger is sensitivity useful when measuring smaller magnetic fields, or when a high accuracy is required. For larger fields, or at lower

accuracy requirements, a smaller sensitivity can be used. Secondly, the Texas Instruments sensor has equal sensitivity in all three directions, while the one from Melexis has a significantly lower sensitivity along the z axis. The z axis thus has a smaller resolution than the x and y axes. In general applications, this does not pose a problem. When one wants to be very exact, it might be more useful to have the same sensitivity in all directions.

During data acquisition, the fluctuations in the measured magnetic field were also monitored and found to be at most $\pm 2.5\mu T$, resulting in a total variation of around $5\mu T$. As discussed in section 3.5, ambient field fluctuations are generally $\pm 2\mu T$ (i.e., $4\mu T$ total). This suggests that the remaining $1\mu T$ of variation is due to current instability in the power supply. This corresponds to the systems design, having an inherent maximal magnetic field fluctuation of approximately $1.2\mu T$.

5.2. 3D magnetic field sweep sensor measurements

5.2.1. Measurement setup and procedure

In the previous sensitivity measurements only 1D magnetic fields were generated. In this section 3D magnetic fields are imposed on the sensors. These measurements utilise the same setup as described in subsection 5.1.1 combined with the LabVIEW 3D magnetic field sweeping script.

For the 3D Helmholtz coil calibration and sensitivity measurements, the primary focus was the slope of the equation describing the test results. The intercept, originating from the ambient magnetic field and possible sensor offset, was removed afterwards. Contrary to this, for the field sweep measurements the slope is not of interest. Instead, the individual data points are analysed. That is why, for each measurement series, the ambient magnetic field was recorded. This was done by placing the sensor in the desired position, and recording the output of the sensors without applying any magnetic field. After the measurements were done, this background field is subtracted for each individual data point to improve the accuracy of the results. This will reduce the error to approximately 1.13% at 2.5 mT.. The individual sensor measurements in the x, y and z direction are compared to the generated magnetic field, and the error is analysed. The error in the angle ϕ (as discussed in section 4.1) provides a more intuitive insight into the deviation of the complete magnetic field vector.

The 3D magnetic field sweeping script is run with fixed axis z and sweeping plane x-y. The sweep is run trough octants $V - VIII$, meaning the z component is always negative. The magnitude of the magnetic field is set to $5mT$, θ is set to 45°, and three steps are taken per octant.

5.2.2. Results 3D sweep sensor measurements

Figure 5.2a and 5.2b depict the relative errors of each data point compared to their expected value for each sensor. The horizontal axis shows the angle throughout the sweep, from 0°to 360°. Note that for both the x and y components two data points are missing. While the absolute errors in these points were not unusual, the ideal values were very small, making the relative error exceptionally large. Including this data would have reduced the clarity of the graphs, and it is difficult to draw any relevant conclusions from such an error. That is why these data points have been disregarded.

Perhaps the most prominent similarity between the two sensors is the error fluctuations in the z component. The z component should stay constant as it is the fixed axis, but it fluctuates sinusoidally. This could be attributed to crosstalk within the sensor (occurring between the z axis and one of the other axes), or the sensor being tilted slightly in either the x or the y direction. However, since this pattern appears consistently across two different sensors, it is more likely that the crosstalk originates from the 3D Helmholtz coil. This results in a small, varying component in the z-direction as the magnetic field vector is rotated in the x-y plane. Comparing this sinusoidal error in the z-direction with the magnetic field measured in the y-direction, as depicted in figures 5.2c and 5.2d, it is evident that the z error is a projection of the y field onto the z axis. This projection can be attributed to the y coil being physically tilted toward the z axis. The small phase shift seen in the z error sinusoid also suggests that the y coil is not only tilted toward z, but likely also slightly toward the x axis.

The relative errors in the x and y axis are less correlated and are often quite large as well. Errors up to -8% are noted for the Melexis sensor, and even up to 15% for the Texas Instruments sensor. Although the magnetic field generated by the Helmholtz coils was expected to have an error maximally 2.3%, this is

frequently exceeded. Moreover, as mentioned before, the steady state field measurements originating from the ambient fields and offset within the device, are removed after the measurements have taken place, so the error would ideally be 1.13% at 2.5 mT. This is clearly not the case. It is possible that the calibration procedure produced incorrect reference values, which lead to computed errors to appear larger than they truly are. The validation of the 3D Helmholtz coil calibration is discussed further in section 5.3.

Another source of error could be that during the field sweep magnetic fields below 2.5mT were created. The magnitude of the 3D vector was chosen to be 5mT, since this is well above the limit of 2.5mT as specified during calibration. However, the x and y components that vary during the sweep are smaller than 2.5mT for certain steps. This in itself is not an error but rather an inherent feature of the field sweep method. However, as mentioned earlier, the offset and ambient field cancellation is brought to mind. Fields below 2.5mT were considered to be less reliable because of the ambient fields, but since these have been (largely) removed, this does not explain errors of -8%, or even 15%. Another possible origin of these errors will be discussed in section 5.3, regarding the response of the sensors to the magnetic field.

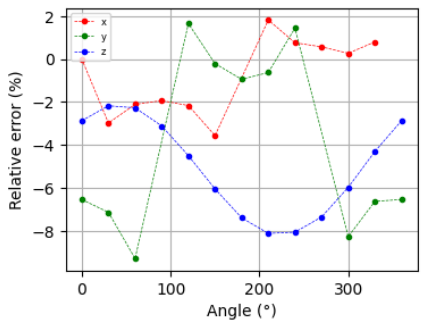

(a) Relative error made by Melexis sensor per data point of the 3D sweep

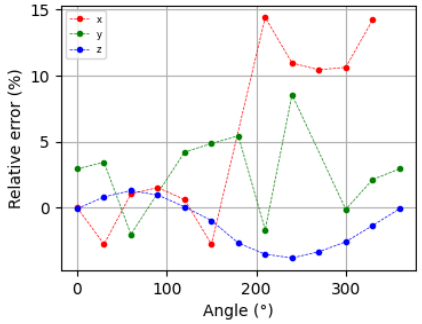

(b) Relative error made by Texas Instruments sensor per data point of the 3D sweep

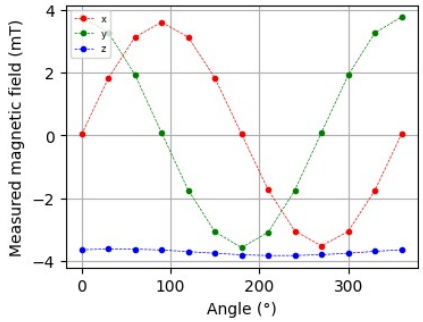

(c) Measured magnetic field Melexis sensor

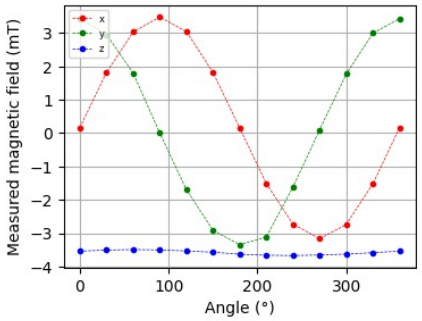

(d) Measured magnetic field Texas Instrument sensor

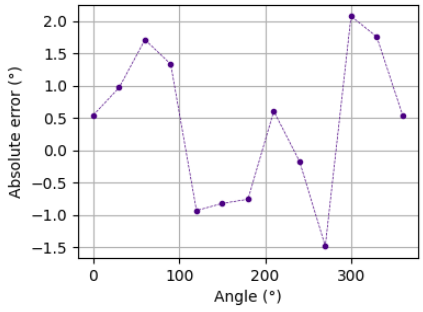

(e) Absolute error in phi for Melexis sensor

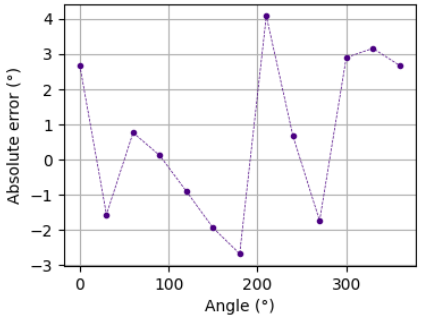

(f) Absolute error in phi for Texas Instruments sensor

Figure 5.2: Errors per data point and errors in phi for the 3D sweep measurements of the Melexis and Texas Instruments sensors

Figures 5.2e and 5.2f depict the absolute error in the angle ϕ (as discussed in section 4.1) for both sensors. This value is calculated using the measured values of the x and y components. There is little correlation between the errors of the two sensors, from which the conclusion can be drawn that the magnetic field script functions correctly and the errors originate from the sensors themselves. Note that the absolute errors made by the Texas Instruments sensor are often larger than those made by the Melexis sensor, similar to the observation made for the relative errors per data point of each sensor.

5.3. Helmholtz coil calibration validation

In this section, the calibration as described in chapter 3 is compared to the calibration data that was provided by the manufacturer Xiamen Dexing Magnet Tech., abbreviated as Xiamen from this point forwards. Since the sensor magnetic field output and applied currents were recorded for both sensors, the same data processing procedure as used for the 3D Helmholtz coil calibration is applied to find the current to magnetic field conversion factors according to the sensors, and see if and how they differ. The main objective is to find out where any potential difference might originate and identify if there is a need for recalibration for better performance. The results of all 4 calibration procedures are given in Table 5.2.

Axis	Xiamen	Calibration	Melexis	Texas Instruments
x	3717.1	3898.0	4005.1	3654.8
y	4118.1	4111.5	4331.8	3933.0
z	4145.5	4037.8	4261.8	4098.6

Table 5.2: Results of 4 different calibration procedures of the 3D Helmholtz coil showing the conversion factors in $\mu T/A$

There are clear differences between the current-to-magnetic field relationships. The differences between the Xiamen and this project's calibration are most likely due the fact that different measurement equipment was used. It is not known what the measurement setup looked during the Xiamen calibration process, and whether the placement of the Gauss meter probe was more, or perhaps less accurate.

More surprising is the large difference in slope between the two sensors. It was not expected that they would produce the exact same output, but since they have undergone the same measurements the slopes were anticipated to be more or less comparable. Since both sensors were placed at the correct height and orientation, this is unlikely to be the source of such large discrepancies. As discussed in subsection 5.1.2, the sensitivity of the Texas Instruments was deemed less suitable for measurements of small fields. Since its measurement range goes up to $\pm 40mT$, fields of 2.5-7mT can certainly be regarded as small fields. However, it is not necessarily so that the Melexis sensor produces slopes that are comparable to those of the manufacturer or this project's calibration. This suggests that the sensors may inherently yield different results, due to the way they are built or internal signal processing mechanisms.

It is observed that the Melexis sensor generally produces higher slope values compared to the calibration results, whereas the Texas Instruments sensor produces lower slopes, with the exception of the z-component. The fact that the deviations from the calibrated values are not consistent across both sensors does not suggest that the calibration procedure itself is flawed. Rather, the calibration results seem to be a reasonable intermediate reference between the two sensor outputs.

5.4. Sensitvity measurements pyramid sensor

As mentioned in section 1.1, this project is carried out to aid the development of the inverted pyramid magnetic sensor, the new 3D Hall effect sensor developed by the MUSIC lab at the TU Delft. A sample of this sensor was been placed in the 3D Helmholtz coil to undergo similar measurements. Subsection 5.4.1 presents the measurement setup and procedure, and subsection 5.4.2 presents the results.

5.4.1. Measurement setup and procedure

A 3D stand, as was created for the commercial sensors, was not available at the time of the measurements. Instead, two wooden sticks were placed horizontally through the coils, upon which the sensor

was placed, at approximately the correct height. The sensor was still situated within the uniform sphere, though the same level of precision as with the 3D printed supports could not be achieved. The wooden sticks were an adequate solution, but it is not ideal for accurate offset or multidimensional measurements where more certainty in the sensor's placement and orientation is required. Since the aim of these measurements is merely to demonstrate the created setup with the pyramid sensor, rather than acquire highly accurate data, this posed no problem in the continuation of the measurements. For future use of the pyramid sensors within the Helmholtz coil, a 3D printed cylindrical stand has been created by the other subgroup. This will make the placement of the sensor much easier, and more accurate.

The readout of the sensor is still analogue, with a dedicated LabVIEW programme that handles the data processing created by J. Ruggeri. This readout provides a whole range of output parameters, from which the output voltage is of interest for sensitivity calculations. This will mean the sensitivity found has the unit V/T, as opposed to LSB/T for the commercial sensors. For each axes, 6 measurement points from 3.5 to 6mT were recorded (5 steps), with an additional measurement zero magnetic field strength applied. These magnetic field strengths were created using the 1D magnitude sweep script developed in chapter 4. For each axis, only one measurement series was performed, as the LabVIEW script for data processing takes an average of 10 measurements.

5.4.2. Results

Figure 5.3 shows, for each axis, the data as found during measurements. The purple data points are the data as given by the LabVIEW data collection script. The offset value at no field applied was subtracted from all values to find the green data points. The resulting linear relationships are shown in the figures as well.

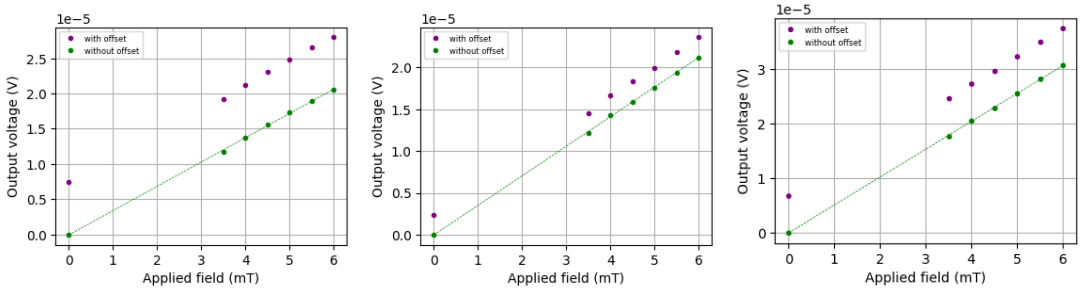

(a) X axis results **(b)** Y axis results **(c)** Z axis results

Figure 5.3: Results of the sensitivity measurements for the pyramid sensor, showing data points with and without offset, and the found slope

Table 5.3 presents the results of the measurements in the form of the sensitivity per axis, compared to the results of the pyramid paper [2], and how much the found values deviate from those of the paper. These are the slopes of the lines as presented in the figures above. The measurements were performed with a constant bias current of $5 \cdot 10^{-5}A$, which is used to find the presented values of the sensitivity from the paper, in which the sensitivities are given in $V/A/T$. Some differences were to be expected in the results, mainly due to the fact that the sensor was not covered during measurements, since a suitable cover for this new set up was not available. Nevertheless, as the main purpose of these tests were to verify the workings of the system with the pyramid sensor, the results are satisfying since they are in the same order of magnitude as the expected values. Especially the z component comes very close to the value as presented in the paper.

Axis	Pyramid paper	Results	Deviation
x	3.66	3.45	5.74%
y	3.70	3.53	4.59%
z	5.15	5.12	0.59%

Table 5.3: Comparison between sensitivity of the pyramid paper and results per axis of the pyramid sensor in $10^{-3}V/T$

6

Discussion

In this chapter, the results of the project are compared to the programme of requirements. The thesis consisted of three chapters concerning the calibration of the Helmholtz coil, the development of a LabVIEW script, and the characterisation of 3D Hall effect sensors. However, in this discussion the choice has been made to combine the discussion of the calibration and characterisation, as their results overlap somewhat.

6.1. Calibration 3D Helmholtz coil and validation with Hall sensors

Requirement 1.1 specifies that the relationship between the current applied to the coils and the magnetic field induced should be obtained. This has been achieved: one conversion factor for each axis was found. Requirements 3.2 and 4.2, which state that each measurement should be performed three times, and with a standard Gauss meter, were also implemented. There was no data exceeding the specified 4% standard deviation, so all measurements were used. During measurements, (magnetic) materials that could affect measurements were placed further away than 0.5m, to comply with requirement 2.1.

Since the uniformity of the magnetic field within the Helmholtz coil is important for reliable measurements, the uniformity within the central 20mm sphere was validated to have at most 1% deviation, in order to satisfy requirement 3.1. The Gauss probe used for the calibration was used for these measurements too, as were the commercial Hall effect sensors. These were compared with the specifications as provided by the manufacturer, and though there were certainly differences in the results, all uniformity errors were well below 1%. Thus, this requirement is satisfied.

Requirement 3.4 states that there should be at most 2% uncertainty in the induced magnetic field within the coils. The largest uncertainty contributor is the ambient magnetic field, ranging from 0 to 50μT. Thus, it is only at a generated magnetic field of 2.5mT that a maximal uncertainty of 2% is achieved. However, when taking other contributing factors into account, such as coil variations and current instability, this amounts to a total relative uncertainty 2.3% at 2.5 mT. So, requirement 3.4 is only fulfilled at 2.87 mT.

Requirement 3.3 states that the magnetic field generated by the coils must be stable to $\pm$1μT for 30 minutes. This requirement refers specifically to the magnetic field generated by the coils, not including ambient field fluctuations. As discussed in section 3.5, current fluctuations of 0.1mA contribute to a maximal fluctuation of $\pm$0.6μT. This stability requirement has been validated in subsection 5.1.2, in which current fluctuations resulting in $\pm$0.5μT magnetic field fluctuations were recorded.

Requirement 3.6 dictates that during sensor characterisation measurements magnetic fields ranging from -7 mT to 7 mT should be applied. However, to satisfy requirement 3.4 it was decided that only magnetic field strength that range from $\pm$2.5-7mT are reliable. This, the sensitivity measurements were performed within this range by taking steps of 0.5mT to get 10 data points per measurement series. 10 steps were chosen, since this provides enough data points to fit a slope to the data points. This also satisfies the second part of requirement 3.6, which states that the increments should be double the

sensor's resolution. Note that the sensitivity measurements were performed by manually controlling the power supply currents, as the LabVIEW script was still under development.

Requirement 1.4 states that sensitivities for each axis of the two commercial sensors should be obtained. Measurements were performed three times, as per requirement 3.2. The resulting sensitivities were comparable to their values as specified in the respective data sheets, though there were discrepancies. These could be sensor orientation errors. To further investigate where these differences come from, further measurements with the sensors could be performed in a zero Gauss chamber.

According to requirement 4.3, the sensor characterisation measurements should be performed using the calibrated Helmholtz coil and LabVIEW 3D sweeping script. The sensor measurement results of the 3D magnetic field sweep had errors in x, y and z components as well as in the angle ϕ that were larger than expected, especially considering the fact that the ambient fields and offset were compensated for in the data processing. All results showed significant discrepancies between the applied field and the field measured by the sensors. These errors revealed that crosstalk occurs during between axes, most likely caused by the z coil being physically tilted toward the z axis. The expected magnetic field strength versus measured magnetic field strengths are not consistent across both sensors, so the results do not suggest that the calibration procedure itself is flawed.

6.2. LabVIEW script

The script successfully meets the core objectives outlined in the programme of requirements. Functional requirement 1.2 specified that the script must execute a 3D magnetic field sweep over user-defined magnetic field ranges and vector orientation across all octants. It must allow the user to choose the sweep resolution and advance each step via a button press. This was achieved by developing a GUI that allows the user to define these field parameters and manually advance through the sweep. To satisfy system requirement 3.5, which states that it must support magnetic field settings from 0 mT to 7 mT on each axis, and be sweepable from 0° to 360° in a user-defined defined plane, the GUI includes all the necessary controls. Due to the power supply's inability to generate negative currents and voltages, a full sweep requires the cables to be reconnected manually each octant. To deal with this, an octant selector was added to the GUI. Additionally, the GUI also includes a control that enables the user to specify at which step number to begin the field sweep, rather than only being able to start from the beginning. This is valuable during long-duration tests where interruptions can occur. Lastly, a static field generation mode was also added, giving users flexibility in experimental setups.

Functional requirement 1.3 mandated that the script must log the current system state, which includes the voltage, current, and magnetic field strength for each coil, at approximately 10-second intervals. Each log must also include a timestamp and be logged in an Excel file. This was achieved with reliable data and timestamps. The functionality was also added for static field use, and logs are generated slightly faster than every 10 seconds.

In support of system requirement 3.3, which states that the magnetic field generated by the coils must be stable to ±1 μT for the duration of 30 minutes, a closed-loop feedback control mechanism was implemented. This solves a power supply hardware limitation which causes a mismatch between the commanded and actual output currents (by approximately 0.1 to 0.5 mA), and mitigates possible current drift due to heating over time.

System requirement 3.4 states that the magnetic field sweep script should operate with a maximum inaccuracy of 2% during sweeps. This was not fully met due to an inherent feature of a field sweep. During a field sweep vector components vary. More specifically, at the edges of each octant in the sweeping plane, one component becomes dominant while the other becomes small, possibly smaller than 2.5 mA. Edge-case accuracy is impacted by the unknown ambient magnetic field.

Additionally, although serial communication with the power supply is reliable, it requires the insertion of 500 ms delays between Write and Read commands to prevent buffer overflow. These delays introduce minor logging delays, with the last data entry lagging $3s$ behind the associated timestamp. Despite this, the script performs as intended with respect to the control of the power supply. It is a robust system, where users can validate results post hoc via detailed logs, operate with confidence within the stability requirements of the system, and resume sweeps.

7

Conclusions and recommendations

7.1. Conclusions

The goal of this project was to develop a system that automates magnetic field generation using a 3D Helmholtz coil. In chapter 3 the 3D Helmholtz coil was calibrated, which resulted in a relationship between the input coil currents and the resulting magnetic field strength at the centre of the coils. It was found that the magnetic field strength of 2.87 mT is the point at which the combined relative uncertainty from ambient field, coil variability, and current fluctuation is maximally 2%. While the generated magnetic field stability is mainly determined by the power supply current fluctuations, which results in a maximal dynamic 1.2 μT fluctuation.

The next stage of the project, discussed in chapter 4, involved developing a control interface that allows users to define arbitrary magnetic field vectors and perform automated 3D magnetic field sweeps. The setup is versatile for characterizing a wide range of sensor behaviours, as it allows the user to specify the sweep resolution, sweeping plane, vector orientation, and magnetic field strength. A range of unplanned but valuable functionalities were added, such as a static field mode, which can be useful when characterising 3D Hall sensors too. The user can also specify at which step number to begin the field sweep, rather than only being able to start from the beginning. This us useful for the long-duration tests which will be performed for the pyramid sensor, where each step can take up to 30 minutes. Lastly, due to the aforementioned hardware limitations of the power supply, and to ensure magnetic field stability, a closed-loop feedback control mechanism was implemented along with the data logging process. Working on the feedback system demonstrated how important it is to understand the limits of the hardware before designing the software.

Finally, in chapter 5 two commercially available Hall sensors were characterised for future comparison with the pyramid Hall sensor. The measurement results revealed that, most likely, crosstalk occurs between the coils, caused by the y coil being physically tilted toward the z axis. Apart from that, the results do not suggest that the calibration procedure itself is flawed.

7.2. Recommendations for future work

There are several ways in which the setup can be improved through negative magnetic field control, improving calibration quality, reduction of environmental noise, and modularisation of code. These possibilities are discussed in the following subsections.

Current polarity control using a H-bridge

A limitation mentioned in section 4.1 is the fact that the power supply can only deliver positive currents and voltages. It is therefore unable to produce magnetic fields that require a negative current, that is to say, negative magnetic fields. If a field in the opposite direction is required, the cables need to be switched around manually. A solution for this is utilising an H-bridge. This is an electronic circuit made up of four switches, that switches the polarity of a voltage applied to a load. Since three outputs of the power supply are used, one H-bridge is needed per output. By controlling which switches are

on/off, the current flowing through the load can be reversed. This way negative magnetic fields can be generated without switching the cables manually.

The LabVIEW code would be adapted, as it no longer has to rely on the front panel ”octant selector.” Instead, the script would keep track which octant it is operating in, and send it to both the *sweep step calculation* subVI and an external Arduino. Communication between the LabVIEW script would take place via serial communication. Based on the table depicted in Figure 4.5, which maps each octant to the appropriate cable connections, the Arduino would then control the H-bridge switches to set the correct current direction through each coil. This automated cable switching system would make the setup more flexible.

3D Gauss probe

Utilising a 3D Gauss probe would significantly improve the accuracy and reliability of measurement results in several ways. Firstly, the probe could be positioned exactly at the centre of the coil system and remain stationary throughout the entire calibration process, including during coil switching. The removal of probe movement between measurements increases repeatability and consistency of measurement results. Secondly, the 3D probe could be used for more reliable uniformity measurements. As tests performed using the 1D probe were limited the probe’s shape and size, and the coils geometry. A differently designed 3D probe could be able to navigate the spaces better and capture more representative field uniformity data. Thirdly, crosstalk detection between coils could be performed, as this is not possible with a 1D probe.

Aside from improving calibration quality, the 3D probe could be used to actively monitor ambient magnetic field fluctuations, which are a major source of uncertainty in the current system. The probe would be placed next to the coil system, and actively measure the ambient magnetic field in all three directions. This data could be integrated into the LabVIEW script. The script would actively adjust the current-to-magnetic field relations to compensate for ambient field variations. This would reduce the uncertainty caused by ambient magnetic field fluctuations. The remaining uncertainty contributors are the fluctuations in each coils current-to-magnetic field relationship (which are not perfectly stable over time) and current supply fluctuations.

Construction of a 3D Helmholtz coil using speaker coils

It would be possible to build a 3D Helmholtz coil system using speaker coils, as described appendix A. This setup could be designed to fit in a zero-Gauss chamber, which removes the background magnetic field. Eliminating this interference would lead to more accurate and precise calibration results. While it is likely that axes misalignments and crosstalk between coils will occur, they can be quantified. This system could then be compared to the 3D Helmholtz coil system.

Potential encapsulation of feedback and logging logic into a subVI

Subsection 4.4.4 discusses that both the static field mode and field sweep mode use the same logic to perform continuous data logging and current feedback correction. However, this has not been encapsulated by a subVI, as the process relies on real-time button presses to advance to the next loop iteration and displays updated values on indicators during the loop. It is possible to turn this into a subVI, but it would require changing te control scheme. SubVIs do not support internal controls like buttons during loop execution. So instead of advancing the sweep based on manual button presses, the system would need to be timer-based, for example automatically progressing every 30 minutes. The code structure was designed to be modular and adaptable, so it is relatively straightforward for future users to adapt it if timing-based control is preferred.

To conclude, this thesis successfully developed an automated test setup for magnetic sensor testing, designed for usability and adaptability in experimental setups. Looking ahead, this system can be used for repeatable magnetic sensor evaluation in research, with a versatility that can benefit various sensor configurations.

Bibliography

[1] Jacopo Ruggeri, Jannik Strube, and Karen M. Dowling. “3D hall-effect magnetometer using a single inverted pyramid structure”. In: *2024 IEEE 37th International Conference on Micro Electro Mechanical Systems (MEMS)* (Jan. 2024), pp. 48–51. DOI: 10.1109/mems58180.2024.10439529.

[2] Jacopo Ruggeri et al. “Inverted Pyramid 3-axis silicon hall-effect magnetic sensor with offset cancellation”. In: *Microsystems amp; Nanoengineering* 11.1 (Feb. 2025). DOI: 10.1038/s41378-025-00876-9.

[3] Shizhong Guo. “Integrated three-dimensional Hall switch sensor based on independent optimized Hall devices”. In: *Microelectronics Journal* 135 (2023), p. 105756. ISSN: 1879-2391. DOI: https://doi.org/10.1016/j.mejo.2023.105756. URL: https://www.sciencedirect.com/science/article/pii/S0026269223000691.

[4] Pavel Ripka (ed). “Magnetic Sensors and Magnetometers”. In: *Measurement Science and Technology* 13.4 (Apr. 2002), p. 645. DOI: 10.1088/0957-0233/13/4/707. URL: https://dx.doi.org/10.1088/0957-0233/13/4/707.

[5] Mohammed Asadullah Khan et al. “Magnetic sensors-A review and recent technologies”. In: *Engineering Research Express* 3.2 (June 2021), p. 022005. DOI: 10.1088/2631-8695/ac0838. URL: https://dx.doi.org/10.1088/2631-8695/ac0838.

[6] Shizhong Guo. “Integrated three-dimensional Hall switch sensor based on independent optimized Hall devices”. In: *Microelectronics Journal* 135 (2023), p. 105756. ISSN: 1879-2391. DOI: https://doi.org/10.1016/j.mejo.2023.105756. URL: https://www.sciencedirect.com/science/article/pii/S0026269223000691.

[7] Konstantinos Papafotis, Dimitris Nikitas, and Paul P. Sotiriadis. “Magnetic Field Sensors’ Calibration: Algorithms’ overview and comparison”. In: *Sensors* 21.16 (Aug. 2021), p. 5288. DOI: 10.3390/s21165288.

[8] C. Wouters et al. “Calibration scheme for a new type of 3D Hall sensor”. In: *Sensors and Actuators A: Physical* 257 (2017), pp. 38–46. ISSN: 0924-4247. DOI: https://doi.org/10.1016/j.sna.2017.02.007. URL: https://www.sciencedirect.com/science/article/pii/S0924424716307531.

[9] Song Zhang and Caihong Li. “Design of a three-axis Helmholtz coil for magnetic sensor calibration”. In: *Academic Journal of Science and Technology* 5.1 (Feb. 2023), pp. 102–111. DOI: 10.54097/ajst.v5i1.5437.

[10] David Henry. “Resistance of a wire as a function of temperature”. In: *The Physics Teacher* 33.2 (Feb. 1995), pp. 96–97. ISSN: 0031-921X. DOI: 10.1119/1.2344149. eprint: https://pubs.aip.org/aapt/pte/article-pdf/33/2/96/11841583/96_1_online.pdf. URL: https://doi.org/10.1119/1.2344149.

[11] Bartington Instruments. *Helmholtz Coil Installation and Calibration*. Accessed: 2025-05-01. Oct. 2019. URL: https://gmw.com/wp-content/uploads/2019/10/Helmholtz-Coil-installation-manual.pdf.

[12] Lars H. Rohwedder. *File:Octant numbers.svg*. URL: https://en.wikipedia.org/wiki/File:Octant_numbers.svg.

[13] *MX100Q & MX100QP Triple Output Multi-Range DC Power Supply Instruction Manual*. Accessed: 2025-05-29. TTi - Thurlby Thandar Instruments. n.d.

[14] *High-Precision 3D Hall-Effect Sensor With I2C Interface*. TMAG5173-Q1. Texas Instruments. 2022. URL: https://www.ti.com/product/TMAG5173-Q1?utm_source=google&utm_medium=cpc&utm_campaign=asc-null-null-GPN_EN-cpc-pf-google-ww_en_cons&utm_content=TMAG5173-Q1&ds_k=TMAG5173-Q1&DCM=yes&gad_source=1&gad_campaignid=1768189849&gbraid=0AAAAAC068F2UbErlNAAtAif4NCyj7aYq7&gclid=CjwKCAjw9anCBhAWEiwAqBJ-c96NrDu0OcD4k7oiEV8c-slK2t9eWwCkahCGG5p3G-_qkitwhSXOJhoC31wQAvD_BwE&gclsrc=aw.ds.

[15] *Triaxis® Magnetic Node*. MLX90393. Melexis. 2024. URL: https://www.melexis.com/en/product/mlx90393/triaxis-micropower-magnetometer.

[16] Webcraft AG. *How do you calculate the magnetic flux density?* URL: https://www.supermagnete.nl/eng/faq/How-do-you-calculate-the-magnetic-flux-density.

[17] 08 Sep 2021. *A quick guide to magnets, Magnetic Metals & non-magnetic metals*. URL: https://www.eclipsemagnetics.com/resources/guides/a-quick-guide-to-magnets-magnetic-metals-and-non-magnetic-metals/.

[18] Gabriel Alberts et al. “On the sensitivity of a laser heterodyne polarimeter for vacuum birefringence detection”. In: *UF Journal of Undergraduate Research* 20.3 (May 2019). DOI: 10.32473/ufjur.v20i3.106302.

[19] Hritwick Banerjee, Shen Shen, and Hongliang Ren. “Magnetically actuated minimally invasive microbots for biomedical applications”. In: *Series in BioEngineering* (Dec. 2017), pp. 11–41. DOI: 10.1007/978-981-10-6035-9_2.

[20] Fawwaz T. Ulaby and Umberto Ravaioli. *Fundamentals of Applied Electromagnetics*. Pearson, 2023.

[21] Encyclopedia Magnetica. *Helmholtz coil*. URL: https://e-magnetica.pl/doku.php/helmholtz_coil.

[22] Michael S Crosser and Gerald J Lynch. “Analytical solution for the magnetic field of a circular current loop in cylindrical coordinates”. In: *American Journal of Physics* 78.3 (2010), pp. 238–245. DOI: 10.1119/1.3258207.

[23] A. Fontanet et al. “Design and construction of 3D helmholtz coil system to Calibrate 3D Hall probes”. In: *Journal of Physics: Conference Series* 1350.1 (Nov. 2019), p. 012167. DOI: 10.1088/1742-6596/1350/1/012167.

[24] Terry Trevino et al. “Design and Build of Electromagnetic HelmHoltz Coils”. In: *51st International Conference on Environmental Systems (ICES)*. ICES-2022-339. St. Paul, Minnesota, July 2022. URL: https://hdl.handle.net/2346/89829.

[25] Malte T. Ahlers et al. “Integration and evaluation of magnetic stimulation in physiology setups”. In: *PLOS ONE* 17.7 (July 2022). DOI: 10.1371/journal.pone.0271765.

A

Permanent magnet vs Helmholtz coil

Magnetic field generation using a permanent magnet

Relying on a permanent magnet to generate magnetic flux offers benefits in terms of simplicity and cost. They are easy to use and do not require a power supply. It has a strong field close to its surface, and the strength of the magnetic field can be varied by changing the distance between the magnet and the sensor. However, as demonstrated by Figure A.1b, the magnetic field produced by a permanent magnet is predominately non-uniform, except for a narrow region along the symmetry axis of the magnet. So when a permanent magnet is used for sensor testing, the sensor should be placed exactly along this axis.

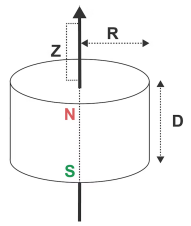

(a) Cylinder magnet [16]

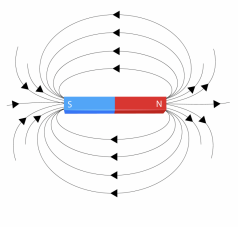

(b) Magnetic field of a permanent magnet [17]

Figure A.1: Structure and magnetic field of a permanent magnet

The magnetic flux density on the symmetry axis of an axially magnetised cylinder magnet is given by Equation A.1 [16], where B_r is the magnet remanence field, z the distance from a pole face on the symmetrical axis, D the thickness of the cylinder and R the radius of the cylinder, as shown in Figure A.1a. As demonstrated by Figure A.2, as distance z increases (moving away from the magnet), the magnetic field strength decays rapidly, while at the surface of the magnet the field is strong and changes non-linearly. This strong distance dependence makes the field highly non-uniform, a small change in position results in a big, non-linear change in magnetic flux density. Despite this, a permanent magnet can provide very strong magnetic fields, ranging from $0.1T$ to $1T$, depending material and size [17].

$$\mathbf{B}_z = \hat{\mathbf{z}} \cdot \frac{B_r}{2} \cdot \left(\frac{D+z}{\sqrt{R^2+(D+z)^2}} - \frac{z}{\sqrt{R^2+z^2}} \right) \tag{A.1}$$

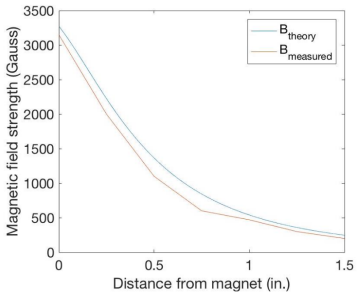

Figure A.2: Plot of magnetic field strength vs distance from a magnet pole for a single N52-neodymium magnet [18]

Magnetic field generation using a one-dimensional Helmholtz coils

Figure A.3 depicts a one-dimensional (1D) Helmholtz coil. The coils are identical, have the same radius and amount of windings, and are positioned parallel to each other on the same axis (the z-axis), at a distance equal to the radius of the circular loops. Figure A.3 also depicts the magnetic field produced by the Helmholtz coil. Outside the loop the magnetic field loops around, while the field between the two coils is approximately uniform.

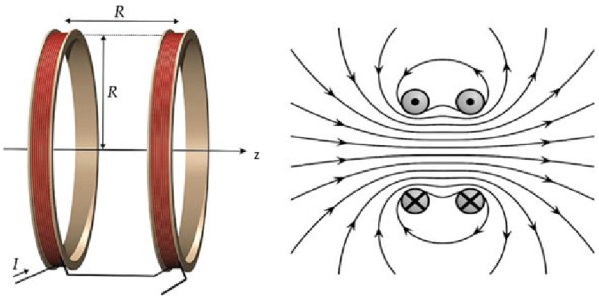

Figure A.3: Structure and the induced magnetic field of a Helmholtz coil pair [19]

The total magnetic flux density of the one-dimensional Helmholtz coil along the z-axis is given by Equation A.2 [20]. The magnetic field along the z-axis is dependant on the current I, the amount of windings N, the radius of the coils a, the permeability of vacuum μ_0, and the position along the z-axis z.

$$\mathbf{B}_{tot}(0,0,z) = \widehat{\mathbf{z}}\frac{\mu_0 \cdot N \cdot I \cdot a^2}{2} \cdot \left(\frac{1}{\sqrt[3/2]{a^2 + (z - \frac{a}{2})^2)}} + \frac{1}{\sqrt[3/2]{a^2 + (z + \frac{a}{2})^2)}}\right) \tag{A.2}$$

The maximum magnitude of the magnetic flux density occurs at $z = 0$, the central point between the two coils, as shown in Equation A.3. Comparing the magnitudes of the magnetic flux density between the two coils demonstrates that the magnetic field between the two coils is relatively uniform.

$$\mathbf{B}_{total}(0,0,0) = \widehat{\mathbf{z}}\left(\frac{4}{5}\right)^{\frac{3}{2}} \frac{\mu_0 \cdot N \cdot I}{R} \approx \widehat{\mathbf{z}} \cdot 0.72 \cdot \frac{\mu_0 \cdot N \cdot I}{R} \tag{A.3}$$

Figure A.4 depicts the magnetic flux density along the z-axis of the Helmholtz coil. It is clear that the magnetic field at the centre is highly uniform. It also demonstrates that the magnitude of the field is maximal in the middle between both coils, and it decreases from the central point to the two sides. The magnetic field is identical on both sides, with the centre acting as symmetry axis.

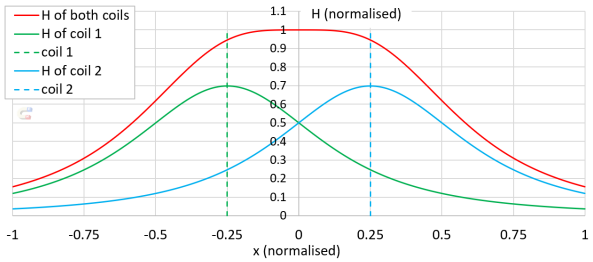

Figure A.4: Field along the axis of a round Helmholtz coil [21]

In the work by Crosser et al. (2010), the authors present a series expansion for the calculation of the magnetic field near the centre of Helmholtz coils [22]. While such calculations are important in understanding the exact magnetic field in between the two coils, it is beyond the scope of this work. We assume an ideal Helmholtz configuration, where the distance between the coils D is equal to their radius R, which delivers maximal uniformity at the centre. Since our application involves placing the sensor at the centre of the coil system, where the field is highly uniform, small misalignments are not expected to significantly affect the field strength or direction.

Magnetic field generation using a three-dimensional Helmholtz coils

Subsection A discussed the operating principle of a one-dimensional Helmholtz coil. The magnetic field generated by this setup is relatively uniform between the two coils, and at the centre of the system it is directed along the axis of the coils and has an intensity given by Equation A.3. A 3D Helmholtz coil generates a magnetic field in any direction, based on the same principle as a 1D Helmholtz coil. In this case, three pairs of 1D Helmholtz coils are are arranged orthogonal to each other [9], as depicted in Figure A.5.

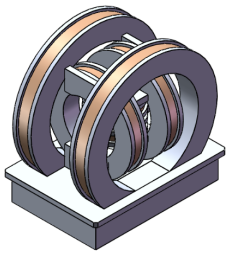

Figure A.5: Drawing of the assembled system of 3D Helmholtz coils [23]

When a current is supplied to the three coils, each Helmholtz coil generates a uniform magnetic field along its respective axis. According to the superposition principle, the total magnetic field at any point is simply the vector sum of the individual fields produced by each coil. Thus, by changing the magnitude and direction of the excitation currents of the three coils, a magnetic field can be generated in any desired direction within the central region of the setup [9]. For a 3D Helmholtz coil, the size of its uniform region can be seen to some extent as the superposition of three pairs of 1D Helmholtz coils in three axes [9]. While the exact shape and size of the resulting uniform field region depends on construction details (coil alignment, radius, and spacing accuracy), the centre of the field is highly uniform in magnitude and direction.

There are physical constraints when arranging multiple coils of the same diameter orthogonally, as the coils would overlap or interfere with each other. Thus, as depicted in Figure A.5, the two additional pairs of coils have to be enlarged with respect to the first one in order to avoid any mechanical interference [24]. Take the z-axis coil pair as the smallest, which sits inside the other two, the y-axis coil pair larger than the x-axis pair, and the x-axis coil pair as the largest, enclosing the other two pairs. Since increasing the radius of the coil alters the magnetic field it produces, the number of turns of the second and third pair of coils must be scaled accordingly to provide the same magnetic field intensity at nominal current [24]. Given that each coil has radius R_i and number of turns N_i, the ratios $\frac{N_i}{R_i}$ must be adjusted

such that the magnitude of the magnetic field intensity of each respective coil pair is equal, so $\frac{N_x}{R_x} = \frac{N_y}{R_y} = \frac{N_z}{R_z}$.

When current is applied to a single-axis coil, the resulting magnetic field produces a projected magnetic field in the other two axes, and the presence of the projected magnetic field affects the data in the other two axes [9]. However, the off-axis magnetic field influences amount to roughly 0.1% of the main contribution [9]. This is a negligible contribution, so the fields generated by different sets of coils can be superimposed [23]. The total field at the origin is then given by the vector sum of the individual contributions of the three 1D Helmholtz coils (described by **??**), and given in Equation A.4. Note that the centre of the three-axial Helmholtz coil is the point where the three orthogonal Helmholtz coil pairs (x-, y-, and z-axes) intersect at a common origin, which is described by coordinates (0,0,0).

$$\mathbf{B}_{total}(0,0,0) = \mathbf{B}_x(0,0,0) + \mathbf{B}_y(0,0,0) + \mathbf{B}_z(0,0,0) = (\frac{4}{5})^{\frac{3}{2}} \cdot \mu_0 \cdot I \cdot (\frac{N_x}{R_x} \cdot \widehat{\mathbf{x}} + \frac{N_y}{R_y} \cdot \widehat{\mathbf{y}} + \frac{N_z}{R_z} \cdot \widehat{\mathbf{z}}) \quad \text{(A.4)}$$

When purchasing a 3D Helmholtz coil, key parameters on the data sheet are *the uniform sphere* and *field uniformity* τ. These paramaters specify the region in which the magnetic field is $100 - \tau$ % uniform. Within this region, a sensor can be placed for calibration, and Equation A.4 can be applied reliably. This relation between the current and the magnetic field forms the basis for the calibration of sensors.

A three-axial Helmholtz coil could also be constructed using three pairs of speaker coils. A speaker coil is a coil of wire that is attached to the apex of a loudspeaker cone, and when a current flows through the coil a magnetic field is generated. These speaker coils can be used to construct the three identical circular coil pairs, where each pair has a different radius and number of turns, as described earlier. Then these pairs of coils are arranged orthogonally, as depicted in Figure A.5. Although this DIY approach has been demonstrated successfully [25], it presents several challenges. Speaker coils are designed to make a loudspeaker cone vibrate back and forth to create sound waves, not to create a highly uniform magnetic field. Furthermore, if the two coils of each pair are not perfectly aligned, the generated magnetic field will display an angular deviation with respect to the nominal axis of the pair and its homogeneity will be degraded [23]. Even small misplacements in spacing or orientation can drastically reduce the uniformity of the magnetic field. While constructing a 3D Helmholtz coil using speaker coils is feasible, it requires perfect alignment and calibration to approach the performance of commercially manufactured setups. Constructing a 3D Helmholtz coil yourself using speaker coils will not deliver a highly precise and uniform magnetic field. It is better to purchase prefabricated 3D Helmholtz coils, as they are constructed more precisely.

B

Standard deviation computations code

```python
import numpy as np

# COIL X - first calibration
slopes = np.array([3880.8, 3847.6, 3902.1, 3934.7 , 3913.6, 3909.2])
mean = slopes.mean()
std_dev = slopes.std()
rel_std_dev = (std_dev / mean) * 100

print(f"Coil X - first calibration:")
print(f"Mean: {mean:.2f}")
print(f"Standard deviation: {std_dev:.2f}")
print(f"Relative standard deviation: {rel_std_dev:.2f}%\n")

# COIL Y
slopes = np.array([4105.8, 4104.3, 4105.2, 4112.4, 4105.3, 4111.4 ])
mean = slopes.mean()
std_dev = slopes.std()
rel_std_dev = (std_dev / mean) * 100

print(f"Coil Y:")
print(f"Mean: {mean:.2f}")
print(f"Standard deviation: {std_dev:.2f}")
print(f"Relative standard deviation: {rel_std_dev:.2f}%\n")

# COIL Z
slopes = np.array([4031.1, 4044.9, 4031.5, 4037.9, 4043.3 , 4036.9])
mean = slopes.mean()
std_dev = slopes.std()
rel_std_dev = (std_dev / mean) * 100

print(f"Coil Z:")
print(f"Mean: {mean:.2f}")
print(f"Standard deviation: {std_dev:.2f}")
print(f"Relative standard deviation: {rel_std_dev:.2f}%")
```

C

Generating magnetic fields below 2.5mT's

As discussed in section 3.3 below the limit of 2.5 mT the relative error created by the ambient field becomes larger than 2 %. However, the coils can still be used in this active region, just with a larger error. During the measurements for the previously presented formulas, fields below 2.5mT were disregarded. However, these measurements are used to quantify how much the formulas differ when using only data points above 2.5mT.

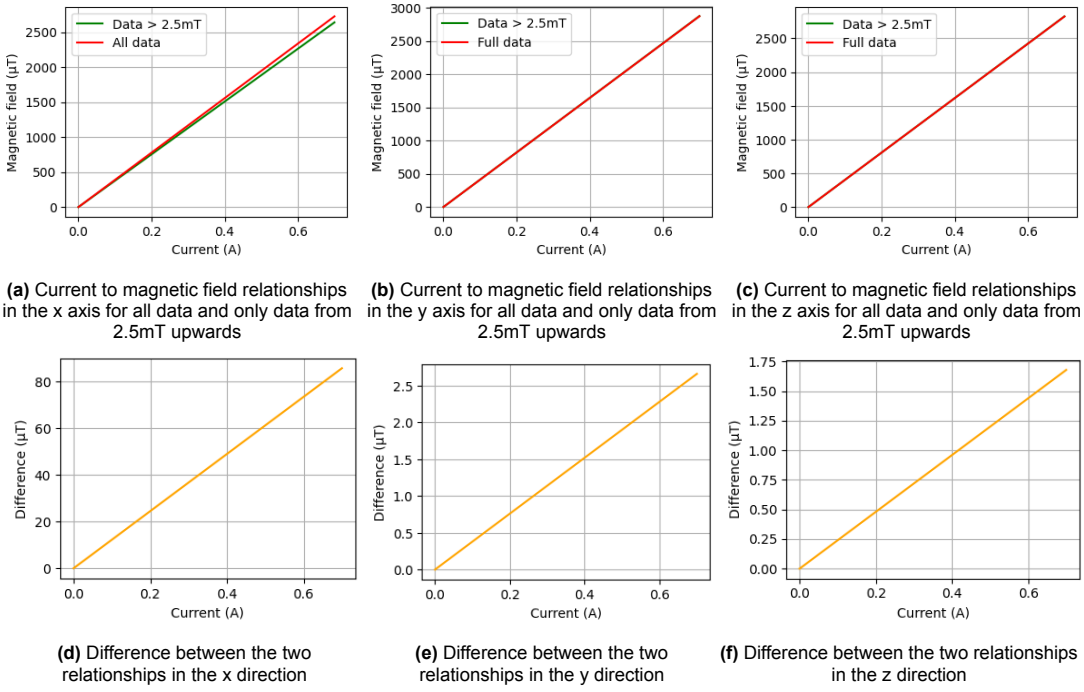

(a) Current to magnetic field relationships in the x axis for all data and only data from 2.5mT upwards

(b) Current to magnetic field relationships in the y axis for all data and only data from 2.5mT upwards

(c) Current to magnetic field relationships in the z axis for all data and only data from 2.5mT upwards

(d) Difference between the two relationships in the x direction

(e) Difference between the two relationships in the y direction

(f) Difference between the two relationships in the z direction

Figure C.1: Differences in current to magnetic field relationships for fields below 2.5mT

Figure C.1 depicts two graphs per coil, only depicting magnetic fields with magnitudes up to 2.5 mT. Figures C.1a, C.1b, and C.1c depict the the results obtained by removing and keeping the measurements under 2.5 mT. Figures C.1d, C.1e, C.1f depict the difference between the two resulting lines. Knowing that the data using only measurements from above 2.5 mT is more reliable, as the relative error of the ambient field is smaller, it is accepted that the green curves show the correct values for the magnetic field. Fort the Y and Z coils the discrepancies are small, while for the X coil the difference be-

tween goes up to 80μT. This is an error of 3.2% at 2.5 mT, clearly larger than the specified maximum error of 2 %.

It is important to note that the results of this analysis may have been vastly different if the measurements were performed in the exact same location, but with the Helmholtz coil turned 90 degrees. The green curves of data larger than 2.5 mT would most likely be very similar, but the background fields might impact the smaller fields in a different manner. Still, the range of error is clearly shown by this comparison. There are large uncertainties, as the difference can be as small as a few μT, and up to multiple tens of μT. In any case, the relationships obtained in subsection 3.3.2 can be used for lower field strengths, though it must be kept in mind that an error well above the specified 2% may occur.

D

LabVIEW code

All the necessary LabVIEW files are accessible on Github at this link: `https://github.com/arepriels/3D-magnetic-field-sweep-LabVIEW-script` .

In order to fully understand the code and the interactions between different modules, it is essential to access and view the code on LabVIEW itself. The LabVIEW code contains annotations throughout, describing its functionality and the reasons behind design choices. Unfortunately, it is not possible to present the full block diagram in the form of screenshots, as LabVIEW doesn't allow for zooming out. Additionally, the number of cases and substructures makes full visual documentation impractical. This chapter will describe one example through series of screenshots. Please see this as an example of the methodology used.

The example presented here are iterations 10 and 11 (which correspond to case 9 and 10, respectively) of the inner for loop within the feedback current control and data logging while loop, operating in static field mode. Note that approximately the same logic is used in the sweep modes, just with less or more loop iterations. This code structure was discussed extensively in subsection 4.4.4. Figures D.1 and D.2 depict a case structure within a for loop, which itself lies in a while loop. The for loop handles handles the data collection, data logging, and current correction. During each iteration of the while loop, i.e. after one complete pass through all 11 for loop iterations, one row of data is written to the spreadsheet file. Each individual for loop iteration appends one value to that row, so each iteration corresponds to a column in the spreadsheet. The case structure within the for loop determines what instructions are executed each iteration, where the first iteration corresponds to case 0, the second iteration to case 1, and so on. Table D.1 depicts the case structure's behaviour.

Figure D.1 depicts case 9 (i.e. iteration 10 of the for loop) of the case statement of the innermost for loop. The block diagram shows the following:

- A query command is generated using the *request current CH3* subVI, which requests the current flowing through channel 3.
- This string is passed on to the VISA Write block, which sends the query to the power supply.
- A small delay of 500ms occurs after this write operation, to prevent buffer overload.
- The power supply's response is read using the VISA Read block. The response string is in the format *x* A (eg. 0.1A), where A is Ampères.
- A string manipulation function is used to remove the A from the response, ensuring that the data is formatted as a number for the spreadsheet.
- This cleaned value is fed to the spreadsheet logging array.
- Simultaneously, this value is passed to the *actual current Z* shift register for use in the following for loop iteration.

Case	Execution
0	The iteration number \textit{N} is logged. If it is the first iteration of the while loop, the startup instructions are sent to the power supply. Otherwise, the \textit{current has stabilized} light is turned on. A $2s$ wait statement is introduced to ensure that the power supply has enough time to execute all the instructions it has received.
1	Timestamp is logged.
2	Voltage CH1 is queried and logged.
3	Current CH1 is queried, logged, and placed on the corresponding shift register.
4	Magnetic field CH1/coil X is calculated and logged.
5	Voltage CH2 is queried and logged.
6	Current CH2 is queried, logged, and placed on the corresponding shift register.
7	Magnetic field CH2/coil Y is calculated and logged.
8	Voltage CH3 is queried and logged.
9	Current CH3 is queried, logged, and placed on the corresponding shift register.
10	Magnetic field CH3/coil Z is calculated and logged. Concurrently, current correction is performed.

Table D.1: Cases of the inner for loop

- The shift registers $I_{set,\,X}$, $I_{set,\,Y}$, and $I_{set,\,Z}$ are set to zero. These values are not used outside this iteration, as only the last value of the for loop is passed to the surrounded while loop via *tunnel mode: last value*.
- A $3s$ wait statement is executed.

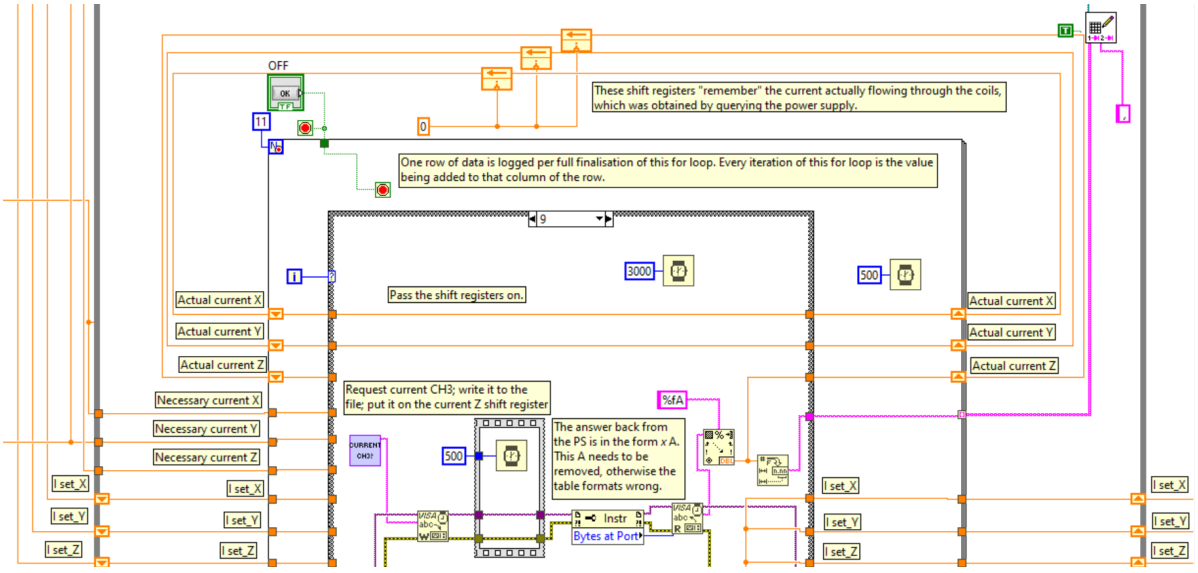

Figure D.1: Case 9 of the case statement within the 11-iteration for loop within the feedback current control and data logging while loop

After this $3s$ delay, the for loop proceeds to iteration 11, i.e. case 10, which is depicted in Figure D.2. The block diagram shows the following:

- The magnetic field of coil Z is calculated using the *Coil current to magnetic field Z* subVI, using the *actual current Z* shift register, which corresponds to the queried current obtained in case 9.
- This calculated magnetic field is fed to the spreadsheet logging array.
- Concurrently, current correction is performed. For each coil, the corrected current is calculated using the *current correction* subVI. The inputs are the queried I_{actual} read from the for loops shift register, the previous I_{set} value (from the while loop shift register), and the required coil current $I_{necessary}$.

- These corrected values are stored in the I_{set} shift registers, for use in the next while loop iteration.
- The command strings containing the new current values are generated using the *current control* subVI's, concatenated, and sent to the power supply using VISA Write.
- A $1s$ wait statement is executed.

After the wait statement is executed, the inner for loop is exited and started again.

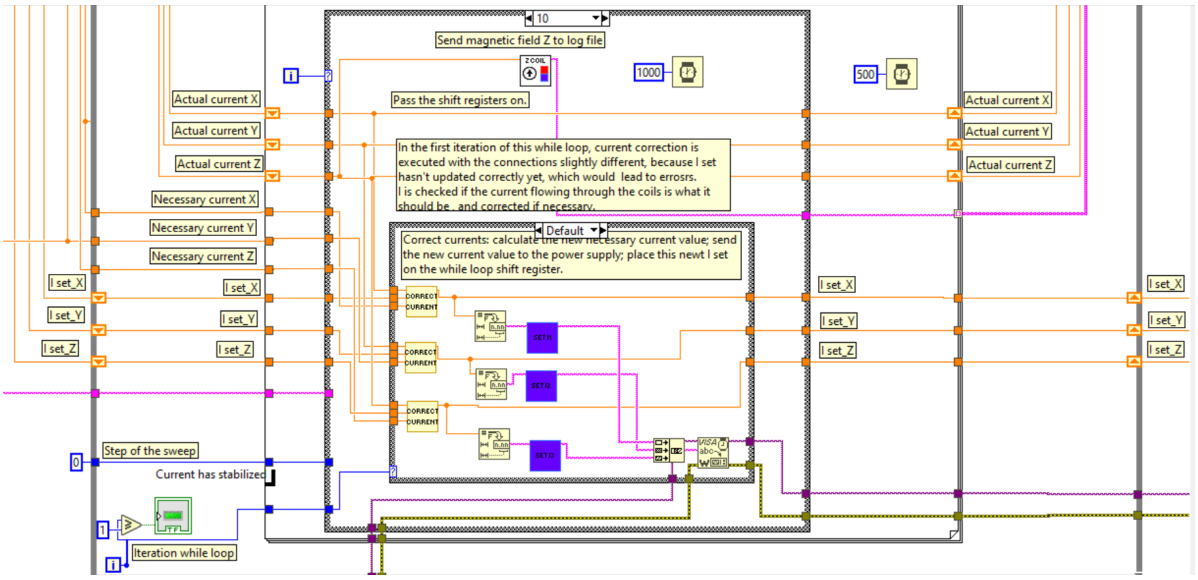

Figure D.2: Case 10 of the case statement within the 11-iteration for loop within the feedback current control and data logging while loop

These two cases gave an overview of two iterations of the current correction and data logging loop. This demonstrated the complex interactions, data dependencies, and real-time communication of the script. For full details on the other cases, and to explore other cases, refer to the annotated LabVIEW block diagram.

E

SubVI's

Driver subVI's for power supply communication

Since the provided driver for the power supply didn't work, numerous subVI's were built to handle communication between LabVIEW and the power supply. These subVI's simplify the formatting command strings to set the voltage limit, set the output voltage, set the current limit, and turn the output channels on or off. Each of these instructions has a specific string format, provided by the power supply manual [13]. For example, setting the output voltage of channel 3 to 2V is done by sending the string *V3\s2\n*. Writing these strings manually in the main script would be error-prone and time-consuming. As it is a repeatable operation, individual subVI's were created for each type of instruction for each channel. These subVI's have a target value as input and as output the command string. The subVI's include:

- Current control: set current limit for CH1, CH2, and CH3.
- Voltage control: set the voltage limits for all channels.
- Channel control: turn all channels on/off simultaneously.
- Query voltage: query the actual voltage on CH1, CH2, and CH3.
- Query current: query the actual current on CH1, CH2, and CH3.

The subVI's were intentionally created individually for each channel to offer flexibility in controlling individual outputs. For convenience, some combined subVI's were created for when simultaneous switching is required. An example is depicted in Figure E.1, which includes the icon and block diagram of the *set current limit CH1* subVI.

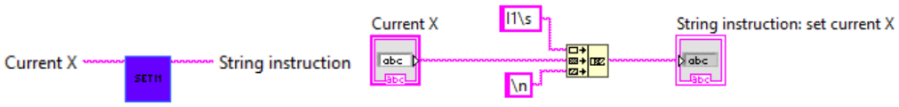

(a) Set current CH1 subVI **(b)** Set current CH1 subVI - block diagram

Figure E.1: Example driver subVI: set current limit CH1

Magnetic field to current conversion subVI's

Each axis of the 3D magnetic field is controlled by a separate coil. As discussed in chapter 3, the magnetic field generated by each coil is linearly related to the current flowing through it. These relationships were determined in section 3.3. Six separate SubVI's (one for each coil and and each conversion type (I $\leftrightarrow$ B)) were created for this purpose, this keeps the conversion parameters separate and easily adjustable for each coil. The magnetic field strength B is given by $a \cdot I$, where a is the slope (given in section 3.3) and I the current. Each subVI has as input the desired magnetic field in µT, and as output the respective required current in A, or the other way round. An example is depicted in Figure E.2, which includes the icon and block diagram of the *magnetic field to current conversion coil X* subVI. Note that the subVI also rounds the output current to the precision used by the power supply.

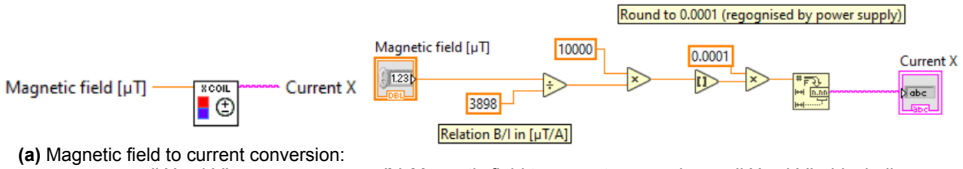

(a) Magnetic field to current conversion: coil X subVI

(b) Magnetic field to current conversion: coil X subVI - block diagram

Figure E.2: Example Magnetic field to current conversion subVI: coil X

1D sweep step calculation subVI

Thus subVI calculates the current value for each iteration of the 1D magnitude sweep based on the user-defined inputs. The inputs of this subVI are the minimum and maximum currents during the sweep, the number of steps *N*, and the current iteration. Equations E.1 and E.2, which were presented in subsection 4.1.1, are used to calculate the necessary current at that step, which is the sole output of the subVI. The subVI and its block diagram are depicted in figure E.3.

$$I_{\text{increment}} = \frac{I_{\text{max}} - I_{\text{min}}}{\text{number of steps}} \tag{E.1}$$

$$I_{\text{step i}} = I_{\text{min}} + i \cdot I_{\text{increment}} \tag{E.2}$$

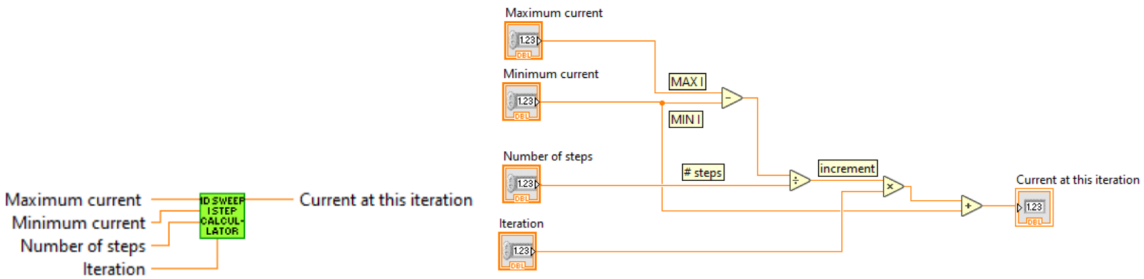

(a) 1D sweep step calculation subVI

(b) 1D sweep step calculation subVI - block diagram

Figure E.3: 1D sweep step calculation subVI

3D field sweep step calculation subVI's

These subVI's perform the calculation of the 3D magnetic field vector for each iteration of the sweep based on the user-defined inputs. The vector math used to maintain constant field magnitude at fixed angle was discussed in section 4.1.

There are two different subVI's used for this purpose, and their structure is independent of the specific sweep plane. Assigning the computed values to the correct spatial components is handled later, depending on the selected sweep plane and octant, according to the table provided in section 4.1.

The inputs of the *3D A and B* subVI are the fixed magnetic field strength in µT, the angle θ from the fixed axis, the total number of steps, and the current iteration, and as output the two magnetic field strengths along the sweeping plane. The *3D C* subVI computes the magnetic field strength along the fixed axis. Since this value remains constant throughout the entire sweep, this SubVI is only called once during initialization. It has only as inputs the fixed field strength in µT, the angle θ from the fixed axis, and the magnetic field strength of the fixed axis as output. The subVI's are depicted in Figure E.2.

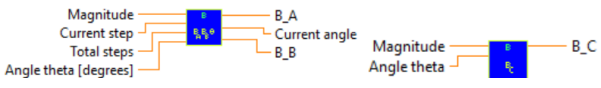

(a) 3D A and B calculator subVI

(b) 3D C calculator

Figure E.4: Sweep step calculation subVI's

As discussed in subsection 4.1.2, the fixed-axis component remains constant, so recalculating it in every iteration is not necessary. So, these SubVIs were intentionally separated instead of combined into a single one with three outputs. By splitting the logic, unnecessary computations are avoided.

Current correction subVI

This subVI calculates the corrected current value that should be sent to the power supply based on the difference between the desired and measured current. It is depicted in Figure E.5 and has as inputs the measured coil current I_{actual}, desired coil current $I_{\text{necessary}}$, and previously set current $I_{\text{set, old}}$, and as output the corrected coil current $I_{\text{set, new}}$. The block diagram is provided in Figure E.5b, and includes a conditional case statement to handle an edge case. Occasionally the power supply returns a small negative current, even when the actual current is zero. To prevent unnecessary correction, the subVI skips correction if the measured current is negative. If the current is positive, the subVI calculates the deviation between the measured and target coil current, and then computes the corrected current value that should be sent to the power supply.

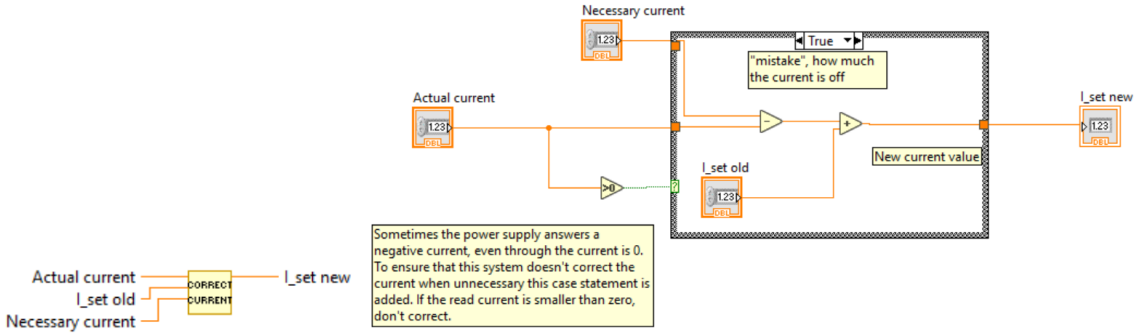

(a) Current correction subVI **(b)** Current correction subVI - block diagram

Figure E.5: Current correction subVI

Static field instruction generator subVI

The main purpose of this subVI is to generate the correct instructions to be sent to the power supply, when the system is in static field mode. These include setting the correct currents (calculated using the *magnetic field to current conversion* subVI's), voltage limits, and turning the channels on. The subVI also has three other outputs, namely the necessary current that should be flowing through each coil (x, y, z). These values are used later on for current correction. The subVI is depicted in Figure E.6.

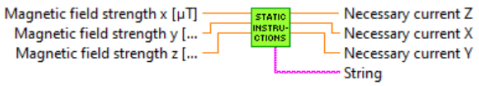

Figure E.6: Static field mode instruction generator subVI

1D sweep iteration instruction generator

The main purpose of this subVI is to generate the correct instructions to be sent to the power supply, at every step of the sweep. It also has four other outputs, namely the current on each channel (x, y, z), and the magnetic field strength along the used axis. The inputs of the subVI are the minimum and maximum magnetic field strengths, direction of the field sweep, current iteration, and number of steps. The subVI is depicted in Figure E.7.

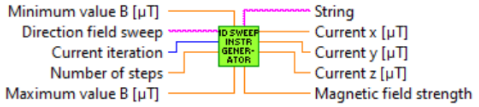

Figure E.7: 1D sweep iteration instruction generator subVI

The subVI consists of case statements with three options: first iteration, next iterations, final iteration. In the first iteration the voltage limits across each channel are set. Next, it checks which axis was selected for the sweep. The currents of the unused axes are set to zero. The start current is applied to the selected coil and that channel is turned on. The required current is calculated using the necessary *magnetic field to current conversion* subVI. The formatting of the instructions being sent to the power supply is done using the *power supply communication* subVI's.
In the following iterations the necessary current values are calculated using the *1D sweep step calculation* subVI, and sent to the power supply using *power supply communication* subVI's. The unused coils corresponding currents remain set to zero.
When all steps have been taken, so at iteration *N+2*, the subVI *turn channels off* is called, which turns all the channels off.

Even though only one power supply channel is turned on, the currents of all 3 channels remain defined. This was done so that the current correction and data logging logic developed for the *static field* and *3D field sweep* modes, which utilize all three channels, could be reused.

3D field sweep iteration instruction generator

The main purpose of this subVI is to generate the correct instructions to be sent to the power supply, at every step of the sweep. It also has four other outputs, namely the angle ϕ, and the resulting magnetic field along each axis (x, y, z). This is necessary, as per the requirements to display the "current state" of the system. The inputs of the subVI are the selected sweep plane and fixed axis, octant, current iteration step,number of steps *N*, magnetic field strength, fixed angle θ, and a *sweep starts later* flag. The subVI is depicted in Figure E.8.

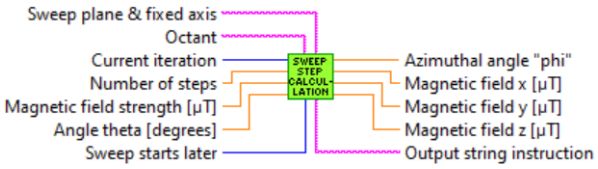

Figure E.8: 3D field sweep iteration instruction generator subVI

The subVI consists of case statements with three options: first iteration, next iterations, final iteration. In the first iteration the *initialisation* subVI is called. First, it sets the voltage limits across each channel. Next, it calculates and applies the correct current to each coil, based on the required magnetic field vector for the first step. Lastly, all the channels are turned on. The required currents for the first iteration are calculated using the *sweep step calculation* and *magnetic field to current conversion* subVI's, the manner in which these are connected being determined by the selected sweep plane and octant. The formatting of the instructions being sent to the power supply is done using the driver subVI's.
In the following iterations the *sweep iteration* subVI is called. This subVI is similar to the *initialisation* subVI described previously and has the same range of inputs and outputs, but it's function is more limited. Unlike the *initialisation* subVI, this module does not set voltage limits or turn on output channels, as these actions are only necessary once at the start of the sweep. However, if the *sweep starts later* flag is set, the sweep begins at a later step instead of step 0. In this case the voltage limits have not been set and channels have not been turned on yet. To account for this, if the flag is high, these instructions are sent too the first step. This separation between the initialization and sweep-step avoids redundant operations.
When all steps have been taken, so at iteration *N+2*, the subVI *turn channels off* is called, which turns all the channels off.